ENHANCING CORROSION RESISTANCE OF STAINLESS STEEL 316 LVM BY VARIOUS SURFACE MODIFICATIONS IN BIOMEDICAL DEVICES

by

Mengnan Guo

Submitted in partial fulfilment of the requirements
for the degree of Master of Science

at

Dalhousie University
Halifax, Nova Scotia
March 2016

TABLE OF CONTENTS

LIST OF TABLES

LIST OF FIGURE

ABSTRACT

Stainless steel is one of the major components for human body implantations which has been utilized to replace bones and stents in human organs. It has been engineered to be corrosion resistance. However, they can still suffer from pitting corrosion. In this study, in order to enhance the corrosion resistance of stainless steel 316 LVM, three various types of surface modifications were used to test the corrosion performance of this alloy in a simulated biomedical device with 0.9 % NaCl solutions.

In situ surface observation, which is associated with optical microscopy, were performed to analyses the samples surfaces before and after corrosion. Ex situ observations with scanning electron microscopy (SEM), energy dispersive X-ray spectroscopy (EDS), atomic force microscopy (AFM) and X-ray photoelectron spectroscopy (XPS) were used to study the difference in sample features and chemical compositions before and after corrosion.

LIST OF ABBREVIATIONS AND SYMBOLS USED

at. %	Percentage atomic concentration
AES	Auger Electron Spectroscopy
AFM	Atomic Force Microscopy
Ag/AgCl	Silver/Silver Chloride
BE	Binding Energy
BSE	Backscattered Electron
CCD	Charge Couple Device
CHA	Concentric Hemispherical Analyzer
Cl^-	Negative Chloride ion
Cr_2O_3	Chromium Oxide
°C	Degree(s) Celsius
DVD	Digital Versatile Disc
EDS	Energy Dispersive X-ray Spectroscopy
EMSI	EllipsoMicroscopy for Surface Imaging
f_0	Resonant frequency of a AFM cantilever
f_s	Area fractions of solid on the surface
f_v	Area fractions of vapor on the surface
fps	Frames Per Second
h	Plank's constant
H^+	Protons

KE	Kinetic Energy
LaB_6	Lanthanum Hexaboride
LED	Light Emitting Diode
LVM	Low vacuum Melt
m_0	Effective massMnS Manganese Sulfide
Mn	Manganese
NaCl	Sodium Chloride (Salt)
S	Sulfur
Pt	Platinum
SS	Stainless Steel
SE	Secondary Electron
SEM	Scanning Electron Microscopy
SiC	Silicon Carbide
UHV	Ultra-High Vacuum
XPS	X-ray Photoelectron Spectroscopy
°	Degree(s)
υ	Frequency of a photon
φ	Work function
γ	Surface tension
γ_{sv}	Solid-vapor surface tension
γ_{sl}	Solid-liquid surface tension

γ_{lv}	Liquid-vapor surface tension
θ	Intrinsic contact angle
θ_w	Apparent contact angle in the Wenzel mode
θ_c	Apparent contact angle in the Cassie mode
θ_s	Intrinsic contact angles of water to the solid

ACKNOWLEDGEMENTS

During my almost two-year study in Dalhousie, I learnt a lot. First of all, I would like to thank my supervisor Harm Rotermund, who offered me a chance to be able to start my life in Canada and also fostered my interest in research, especially in corrosion science.

I would also like to thank my previous co-worker, Alisina Toloei, who guided me through my research and helped me overcome lots of difficulties, including conducting experiments and writing papers.

Besides, special thanks goes to Peter Klages, who helped me a lot and offered knowledgeable information and discussions about the experimental set ups in the lab, which certainly made it easier for me to start using the techniques.

Finally, I would like to thank anyone who offered me a helping hand in my studies and life. Special thanks goes to my parents who supported me all the way throughout my life.

CHAPTER 1 INTRODUCTION

Stainless steels are generally designed to be highly resistant to general corrosion; yet it is likely for stainless steel to suffer from localized corrosion. The two major forms of localized corrosion consist of pitting and crevice corrosion. Under both of these two situations, the attack is limited within small areas of the surface while the remaining surface is unaffected [1]. The perforation generated by pits could further increase cracks, which are initiated at the base of the pits due to the fact that fatigue and stress corrosion cracking may lead to failures of the structural integrity of the material itself. Since stainless steels are widely used in industry facilities and biomedical devices, this phenomenon of corrosion can cause permanent damage or health issues in terms of the corrosion products from biological implants.

In order to prevent a possible catastrophic failure caused by pitting corrosion, a thorough understanding of the mechanisms and interactions in terms of pitting sites at early stages of development is required. Optical *in-situ* observations are of vital importance, and allow the non-destructive visualization of the surface to detect the onset of any metastable pitting events. In this way, a clear and vivid picture of the processes happening on the surface of the material will be obtained. In addition, ex-situ surface analysis utilizing scanning electron microscopy (SEM), energy dispersive spectroscopy, atomic force microscopy and X-ray photoemission spectroscopy to name a few, also allow one to develop a general observation on the depth of the pits, determination of chemical elements and compounds. The combination of these *in-situ* and *ex-situ* methods of surface investigations provide a better way for the

understanding of the corrosive events taking place in the early stages on the surface of the material itself.

In this research work, three interrelated projects have been developed and proceeded simultaneously to study metastable pitting *in situ* and to deduct the degree of pitting corrosion on stainless steel 316LVM in saline solutions. Results from the first two projects have been submitted to peer-reviewed journals. Also, each of the articles associated with the first two projects and the results obtained from the third project constitute one of the chapters to follow. Additional information in terms of each project will also be provided. The first project is primarily concerned with the effect of morphology of the surface in terms of the corrosion performance of stainless steels 316 LVM in biomedical environment. Unidirectional surface smoothness was created by grinding the surface with SiC papers with different radius parameters of the particles. In total, five types of surface morphology were produced. By using in-situ background subtracted contrast-enhanced microscopy, the difference between the surface before and after corrosion for surfaces with different degrees of smoothness becomes obvious. The second project describes a way to further enhance the corrosion performance of the stainless steels in the same saline electrolyte used in the first project. Two styles of surface topographies have been created on the end faces of stainless steel wires to test their corrosion resistance as implanted biomedical devices. Stainless steel 316 LVM wire was initially ground flat with 115 μm grit SiC paper, then polished with successively smaller grit SiC paper to 53 μm, followed by 16, 5 and 3 μm to create the smoothest (G1500) surface finish before treatment to produce two different topographies 1.) Unidirectional roughness was created using SiC papers and 2.)

Various patterns created with specific hole diameter and inter-hole spacing using a focused ion beam (FIB). The in-situ optical techniques described in the first part were used to confirm that corrosion occurs only on the polished surface due to localized pitting events. Scanning electron microscopy and energy dispersive X-ray spectroscopy were used as ex-situ techniques for compositional determinations of the stainless steel. The third project explores the effect on the nano-pure water treatment on the corrosion performance of stainless steel 316 LVM. Samples underwent the same grinding process and ended up with five types of surface finishes before conducting high temperature water treatment on the surface. For comparison, the corrosive resistance of the water-treated and non-water treated samples were compared by the initiation time of pitting, stable pitting potential and critical current. In the following chapters, detailed introduction about each project will be described.

These three projects demonstrate the capability of the enhancement on corrosion resistance of stainless steel 316 LVM by surface modifications with regards to the improvement on surface smoothness, surface patterns and water treatment. The coherent trend of increasing pitting potentials, the decreasing of critical current and initiation time for pitting corrosion obtained from electrochemical tests verify the fact of a better corrosion performance of stainless steels. The projects were successful; they also serve as starting points for new investigations into pitting corrosion and in better utilization of in-situ optical techniques. Meanwhile, they provide a better understanding about the pitting processes based on surface analysis and visualization with both in-situ and ex-situ techniques.

1.1 INTRODUCTION TO PITTING CORROSION

Pitting corrosion is one of the highly localized forms of corrosion. Pits are normally initiated within specific constrained small areas, and proceed with perforations which causes stress to the material itself [2]. Pitting occurs due to the localized breakdown of a passive film on the surface of the material, and is normally induced by chloride ions, but the presence of various other types of ions, such as Br^-, I^-, SO^{2-}, or NO^{3-} can also contribute to the pitting events [3].

Pitting is considered as one of the most dangerous forms of corrosion in several aspects. One of the reasons can be attributed to the fact that perforation is generated by pits, but the remaining part of the metal remains untouched [3]. Furthermore, these small perforated pits can serve as critical sites to initiate stress-corrosion cracking in the following stages, which is often considered as one of the catastrophic forms of corrosion. Finally, the detection of the earliest stages of pitting events can be relatively difficult if the pits are covered with corrosion products.

The chloride ions have exerted much more importance in pitting corrosion for several reasons. First of all, chloride ions are ubiquitous, constituting seawater, found on airborne particles, in de-icing water, and brackish water [3], which is the type of water having a higher degree of salinity than fresh water, but not as much as seawater. Moreover, chloride ions are the major components included inside the human body environment, which can easily cause corrosion phenomena on biomedical implants. Also, chloride ions are classified as Lewis base (electron donor), which are more likely to interact with Lewis acid (electron acceptors), for instance the metal cations. This

phenomenon has been shown in Figure 1.1 below. The last possible reason can be the fact that chloride ions are relatively small ions with higher diffusivity.

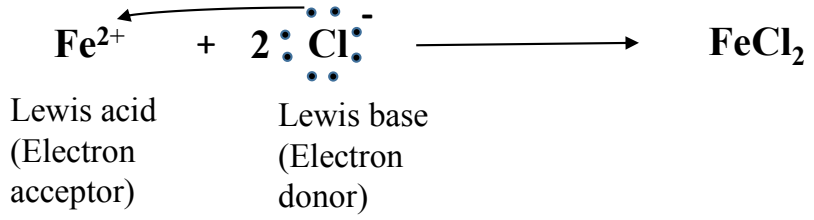

Figure 1.1 Lewis acid and base interactions.

Corrosion is both a thermodynamic and kinetic process and related to quite a few factors. One of the factors can be attributed directly to the intrinsic property of the metal itself. The oxidizing metal cations are more susceptible to the attack from corrosion. Under this scope, the metallurgical factor which is associated with the types and the amount of the chemical elements embedded within the major components of the metal, does have an effect on the performance of the metal or alloys. For instance, the addition of chromium, nickel, molybdenum, and nitrogen enhances the pitting corrosion resistance of stainless steel alloys [4–10]. Another broad range of factors, which affects pitting, can be attributed to external ones. Temperatures, concentration of the corrosive solutions, composition of corrosive solutions, pH of the corrosive environment, and the inhibitors used are of vital importance to alter the pitting resistance of the metal or the alloys [3]. The halides and halogen-containing anions, such as chlorides, bromides, and hypochlorite, are among the most aggressive species of halogen-containing anions [1]. In this research, in order to mimic the biomedical environment inside human body, sodium chloride (NaCl) was chosen as the corrosive electrolyte.

1.1.1 Mechanism of Pit Initiation

Generally speaking, pitting corrosion can be divided into two major stages, pit initiation and propagation. The initiation stage associates with both the breakdown of passive film on the surface and the onset of the anodic current [3]. There is no precise understanding about the mechanism of pitting. However, the basics ideas have been understood. Three major mechanisms have been proposed [11–14]. They are (i) the penetration mechanism, (ii) the film thinning mechanism (absorption mechanism), (iii) the film rupture mechanism.

The penetration mechanism states the fact that Cl^- ions penetrated through the oxide films to reach the surface of the bulk of the metal where the localized dissolution is promoted [13]. The migration and diffusion of anions will be enhanced if there is an external electric field. Marcus and Herbelin found chloride present in passive films on Ni using careful XPS and radiotracer measurements [15], indicating that a critical concentration of chloride in the inner oxide portion of the passive film was associated with film breakdown and pit initiation. The penetration mechanism is depicted in Figure 1.2.

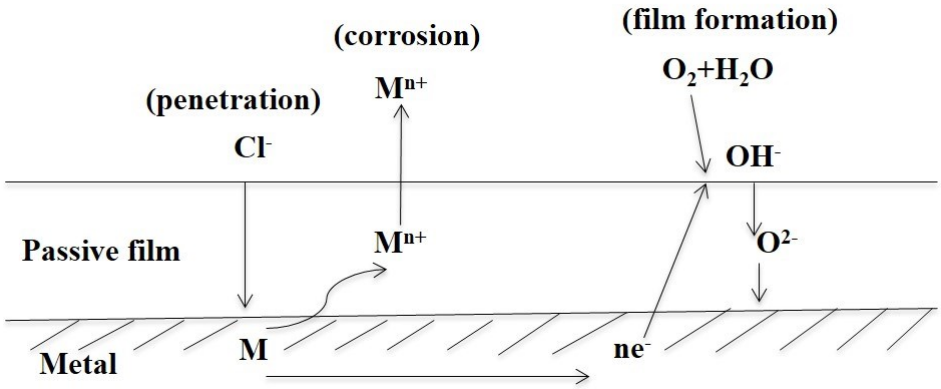

Figure 1.2 The penetration mechanism of pitting corrosion including penetration formation of corrosion products and film formation [3,13].

Macdonald and his co-workers proposed a point defect model for the breakdown of the passive film [16,17]. The assumption in this model is that the vacancies caused by the outward migration of cations would move inward from the interface of oxide/electrolyte. As time went by, the voids due to the accumulation of condensed vacancy at the metal/oxide interface would lead to the stresses on the interface of metal and passive films, which initiate the pitting [3].

In the film thinning mechanism (absorption mechanism), the first step is the absorption of aggressive ions on the metal/oxide interface. This absorption leads to the probability of formation of surface complexes or clusters, which further cause the local dissolution and thinning of the passive layers [3], as shown in the Figure 1.3. Strehblow et al. showed that due to the catalytically enhanced transfer of cations from the oxide to the electrolyte, the exposure of Fe to the Cl^- and other halides caused the thinning of the passive layers from the XPS measurements [18]. Once the initiation of thinning starts as a result from locally absorbed species on the passive layers, the local electric field will increase, eventually causing the breakdown of the passive layers and formation of pits [13]. XPS measurements have shown that halides, such as F-, Cl-, Br-, and I-, all can lead to the thinning of passive layers on iron [19].

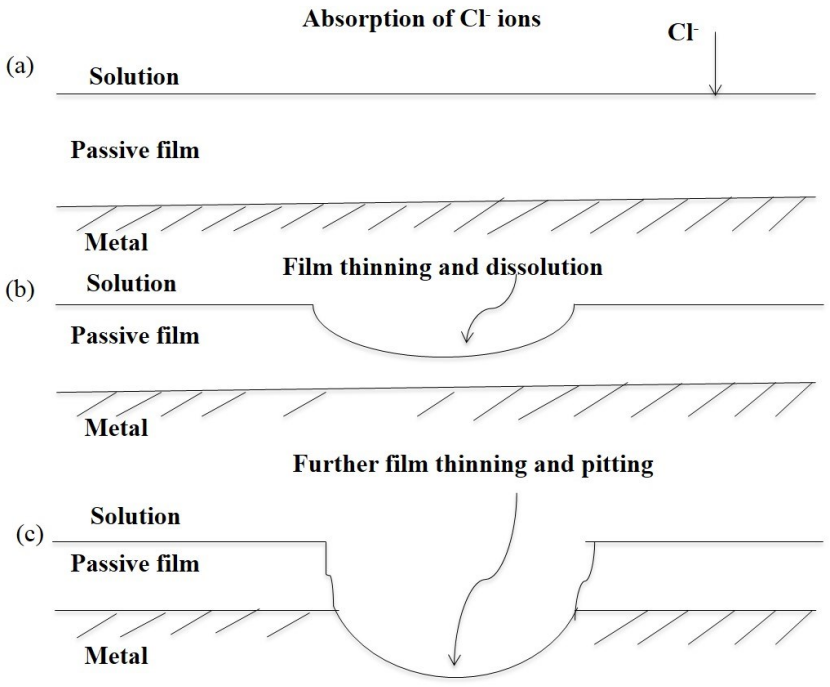

Figure 1.3 The film thinning mechanism (absorption mechanism) of pitting corrosion [3, 13]. (a) Initiation of absorption of on the Cl- surface of passive films. (b) Continuous thinning of the film. (c) Pitting starts.

The third proposed mechanism is the film rupture mechanism; aggressive ions approach the bulk metal surface through surface defects, such as cracks, flaws or inclusions. For instance, the inclusions that will be attacked on the stainless steel surface are manganese sulfide [20–23]. Defects may be further developed by the hydration/dehydration process in the oxide films due to the invasion of Cl^- ions into the film [3]. The breakdown and repair of the passive films on the surface of the metal can be considered as continuous states, which can be thermodynamically balanced if, the rate of both the reformation and breakdown of passive layers can be the same [24,25]. In chloride-containing solutions, it is less likely for the breakdown of the passive film

to be repaired [13]. The following Figure 1.4 illustrated the film rupture mechanism [3,13].

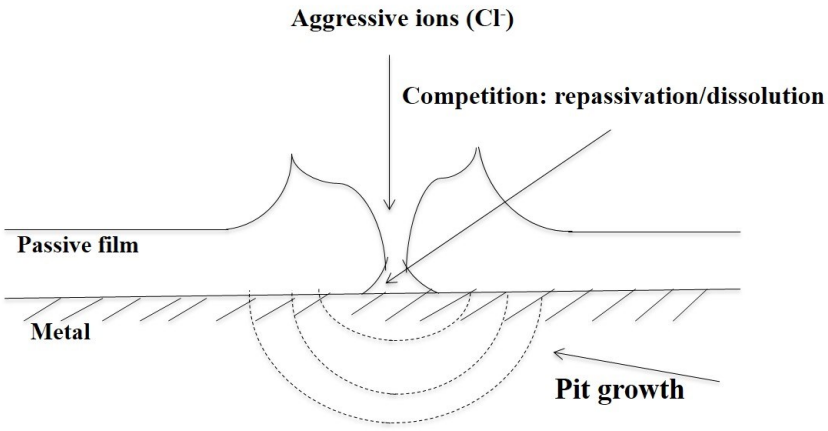

Figure 1.4 Film rupture mechanism of pitting.

1.1.2 Mechanism of Pit Propagation

The mechanism of pit propagation will be illustrated in Figure 1.5. When propagation starts, the local critical current density associated with pitting is very high due to the confinement of the geometry of the pits, which are generally tens to hundreds of microns in depth [3]. At the first stages of propagation, the passive films adjacent to pits will be untouched. Initially, the size of the pits is relatively small. As with the progress of pitting, the volume of pits increase. However, compared with the bulk of the material, there is still a geometrical limit for the dissolution of metal cations.

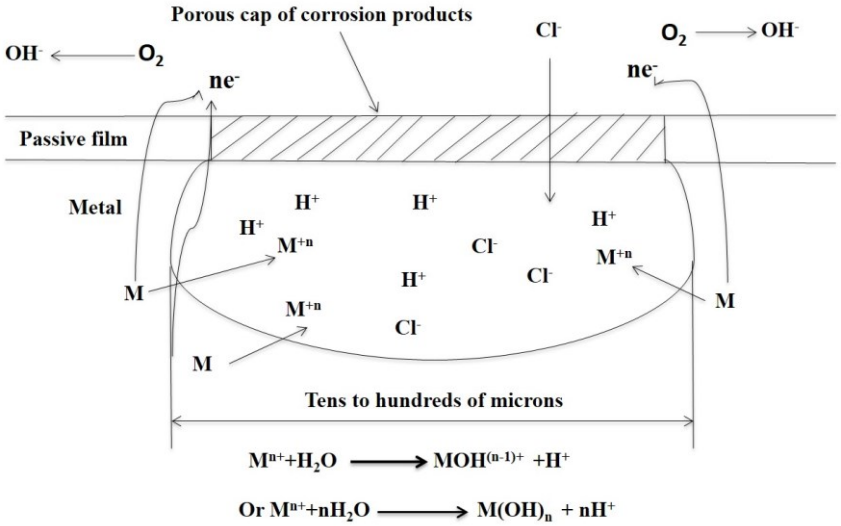

Figure 1.5 Simple illustration of propagation stage of pitting [3].

Consequently, the accumulated metal cations undergo hydrolysis, producing protons (H^+) and increasing the local acidity inside the pits. The Cl^- ions migrate from the bulk of the solution into the confined place of pits so as to maintain charge neutrality within the pit solution.

Pitting corrosion is an electrochemical oxidation-reduction process, which occurs within localized deeps on the surface of metals coated with a passive film. The associated electrochemical reactions are listed below [3]. Anodic reactions inside a pit:

$$Fe=Fe^{2+} + 2e^- \text{ (dissolution of iron)}$$

The electrons which are produced from anode will flow to the cathode, which locates on the sample surface, and involve in the oxygen reduction reaction:

$$½\ O_2 + H_2O + 2e^- = 2(OH^-)$$

As a result, the electrolyte enclosed in the pit gains positive electrical charge in contrast to the electrolyte surrounding the pit, which becomes negatively charged. In order to maintain the electrically neutrality of the solution inside the pit, chloride ions will be attracted inside the pit, and participate in the following reaction.

$$FeCl_2 + 2H_2O = Fe(OH)_2 + 2HCl$$

Acidity of the solutions inside the pit increases, and the pH of the electrolyte inside the pit decreases from 6 to 2-3, which causes further acceleration of corrosion process. A large ratio between the anode and cathode areas favors increase of the corrosion rate. Corrosion products ($Fe(OH)_3$) will form around the pit.

1.2 HISTORICAL REVIEW OF STAINLESS STEEL

Stainless steels, one of the world most widely used alloys nowadays, is also one aof the significant achievement of modern metallurgy[26]. It has been described as " miracle metal" and " crowning achievement of metallurgy" by the famous 20th century metallurgist Carl Zapffe [26]. The earliest discovery can be traced back to 18th and 19th centuries, with the identification of chromium as one of its major components [26]. Léon Guillet was the first to metallurgically investigate chromium and chromium steels with various types of crystalline structure [26]. However, he barely did work on the research of corrosion resistance of these steels. Pierre Berthier experimented with iron alloy compositions in 1821 with high chromium content alloys, following the experiment conducted by Faraday and Stodart [26,27]. Due to the large amount of carbon contained in the sample alloys, the resistance towards oxidation was quite low. Misunderstanding about the inefficient corrosion resistance were attributed to the high chromium contents [26]. Only until 1898, did A. Carnot and E. Goutal report in their discovery that high carbon contents would have a detrimental effect on the corrosion resistance of iron-chromium alloys [3,26]. Later, in 1908, German scientist Philips Monnatz investigated the effect of carbon content related with the corrosion resistance

of high-chromium steels. Monnatz was claimed to be the first to realize the fact why stainless steels were stainless [26]. Specifically, he was the first to determine the vital effect of high chromium content in stainless steels. Also, he discovered that free carbides or carbide precipitations were detrimental to the corrosion performance of steel alloys. There are so many twists and turns in the development and understanding about the structures and corrosion performance of various types of stainless steel alloys [3,26,27].

The actual commercialization of stainless steel started to boom simultaneously in France, Germany, England, and the United States in 1912. Nowadays, hundreds of thousands of products associated with stainless steel alloys, such as medical implants, building materials, nuclear reactors and industrial vessels, are created.

In our work, low carbon stainless steel 316 LVM were investigated. Table 1.1 shows the general details of major elements determined by Energy Dispersive X-ray Analysis [20].

Table 1.1 Chemical compositions of stainless steels; major elements determined by EDX [28].

Stainless steel (AISI)	Cr	Ni	Mo	Mn	Si	C	P	S
316 LVM	18.2	14.6	2.85	2.61	0.7	≤0.025	≤0.003	≤0.003
316 L	16.6	12.3	2.03	2.26	0.6	0.04-0.08	≤0.045	0.006-0.03
304L	18.1	9.3	<0.02	1.95	1.35	0.04-0.08	≤0.045	0.003-0.03

The corrosion resistance of stainless steel originates from its naturally formed passive oxide film on the surface which acts as a protective barriers against the

aggressive ions in the environment [29]. The nature of the passive layers is complex; often, it is a mixture of metal oxides and hydroxides [3]. From one of the early analyses of passive layers by X-ray photoelectron spectroscopy (XPS) [30] of type 304 stainless steel, it was reported that the major components within the passive layers consisted of oxides with Cr and Ni, and Fe. Additionally, Cr^{3+} constituted the majority part of the region related with the outer region of the passive film, whereas the inner and outer regions both contained Cr^{3+} and Ni^{2+}. More recently, studies with regards to XPS analysis of the passive layers of stainless steel, which contained Mo as one of the alloying elements, showed that Mo^{4+} was found in the inner region of the passive films, and Mo^{6+} was located in the outer regions [18]. It was suggested that the chemical compounds (oxides and hydroxides) formed in terms of Cr, Ni and Mo would enhance the properties and performance of resistance of the thin film [4–6] . It is obvious that stainless steel 316 LVM has relatively high chromium, nickel and molybdenum content compared with the other two types listed in the Table, indicating a better corrosion performance.

Despite of the fact those stainless steels are resistant to general corrosion, they are susceptible to localized corrosion in terms of crevice and pitting corrosion. Generally speaking, if the passive layer is capable to undergo the reformation process in the initial stages, then the early-formed micro pits will tend to be less harmful to the metal itself. However, if the steady state of the breakdown and reformation of passive layers is disturbed in the early stages, as in most of the cases, localized corrosion occurs. It is generally acknowledged that surface inhomogeneous sites, such as inclusions, defects, scratches and crevices, are the critical places for the initiation of pitting

corrosion [2,31]. The most common aggressive ions that trigger pitting events on stainless steel alloys are halide ions and specifically chloride ions (Cl^-) [1]. In low carbon stainless steel alloys, as it is associated with the research work presented in the thesis[22], it has been reported that sulfide inclusions, especially MnS, have an influential effects on the initiation of pitting [20–23]. However, stainless steels with carbon content larger than 0.1%, the key factor that starts the onset of pitting corrosion, is related to the formation of carbides [32]. The formation of carbides is due to the combination of carbon and chromium at grain boundaries, which deplete chromium and decrease the capability of passive layers against corrosion [27].

Efforts have been made to improve the corrosion resistance of stainless steels alloys. Several possible methods have been proposed, which can be sorted in the following categories. First, one can be attributed to alloying and increasing the content of specific beneficial elements, such as Cr, Ni, Mo, and N [4,5,8–10]. Another method to enhance corrosion resistance is surface modification [33–37], such as creating surface organic inhibitors, laser treatment, modification of surface oxides. In this research, simple mechanical surface modification with grinding and high temperature water treatment was applied to stainless steel 316 LVM samples.

1.3 INTRODUCTION TO THE EXPERIMENTAL SET-UPS

1.3.1 Equipment Used in Electrochemical Tests

In our study, the purpose of the research is to delay the initiation and degree of corrosion on the surface of stainless steel 316 LVM samples in the early stages of pitting corrosion. In total, two major types of tests have been performed on the samples,

which are electrochemical tests and surface analysis. A three-electrode electrochemical cell was used to conduct the experiment. The sample itself is the working electrode, platinum wire acts as a counter electrode, and silver/silver chloride serves as a reference electrode. In order to simulate the inner human body environment, 0.9% by weight sodium chloride (NaCl) solutions was used. Figure 1.6 illustrates this electrochemical cell. This cuvette was placed on the small platform where adjustments could be made to suit the optical pathways for the optical set ups.

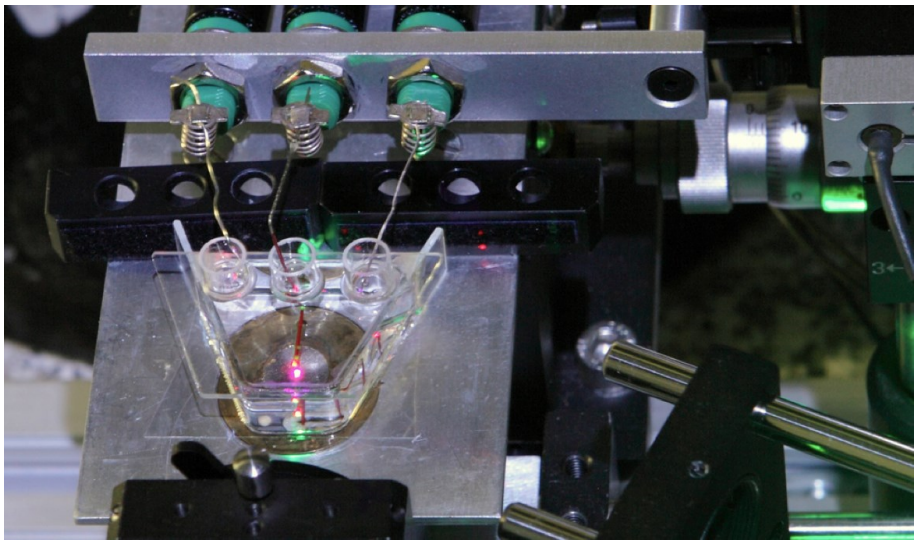

Figure 1.6 An illustration of a three-electrode cell used in the corrosion tests.

A three-electrode system includes three electrodes, which are working electrode, reference electrode, and counter electrode. The reason for adopting a three electrode system is based on the fact that the potential on the electrode depends on the current flows through it. In a two electrode system, the polarization on both reference and working electrode lead to the potential drop (IR drop) that originates from the resistance of the solutions between reference and working electrode [38]. Hence, a two-electrode system will provide a non-linear response with a small linear range [39]. The

addition of a third electrode, which is the counter electrode, enables the majority of the current flows through the counter electrode, leaving only a negligible amount of current passes through the reference electrode. By doing this, the potential shift on the reference electrode can be ignored. A schematic diagram of a three-electrode system was shown in Figure 1.7 below.

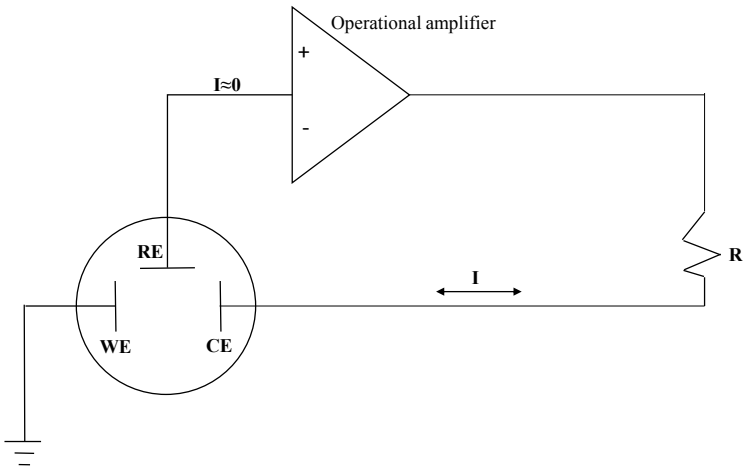

Figure 1.7 A schematic diagram of a three-electrode system.

The operational amplifier is used to make sure that almost no current flows through the reference electrode so that there is no loss from the initial potential (E_{in}) which was supplied from the operational amplifier. The role of the reference electrode is measuring and controlling the potential on working electrode. The counter electrode passes all the current needed to balance and it also measures current at the working electrode. The glass cuvette is specially engineered to fit the optical set ups, which will be described later. The cuvettes used were made from flat pieces of glasses glued tightly together so as to be perpendicular to the optical pathway for microscope. Junctions among different glasses were heavily glued to avoid leakage. The actual physical height of the cuvette is around 1cm. This cuvette size would allow 2 μm lateral for the sample

stainless steel wire. In order to ensure the clear optical imaging, the cuvette needs to be cleaned with nano-pure water after each experiment, and 4 separate pieces of glass on a coverslip were fragile. The shape of the cuvette was formed by Andy George who bent the glass with caution over the fire block molds, which has been illustrated in Figure 1.8 [40].

Figure 1.8 Bending process was preceded with hydrogen-oxygen flames to form the shape of the cuvette.

Stresses were introduced to glasses after the bending procedure, which would certainly affect the polarization of the light. Annealing was applied to the glass by

heating the glasses at 3 °C/min to 500 °C, and the duration of this constant-temperature annealing was 5 hours [40]. After annealing, glasses were cooling down at a rate of 3 °C/min. Edge-polishing was done after bending the glasses to create flat seams for gluing later.

The top of the cuvette was attached with a lid that held three openings for three different electrodes. The structure of the cuvette is presented in Figure 1.9 above. Measurements have been made to determine the actual lengths of the cuvette. The lengths of back face and front face of the trapezoid are 30 mm and 11 mm. The distance from the bottom piece of glass to the front face is 20 mm, which ensures a total surface area of the trapezoid to be 410 mm^2. The total height between the bottoms to the glass lid is 11.37 mm. The thickness of the base, lid and sidewalls are 0.15 mm, 1.08 mm and 1.06 mm, respectively. Figure 1.9 and Figure 1.10 shows the real image and information of the dimensions of the cuvette.

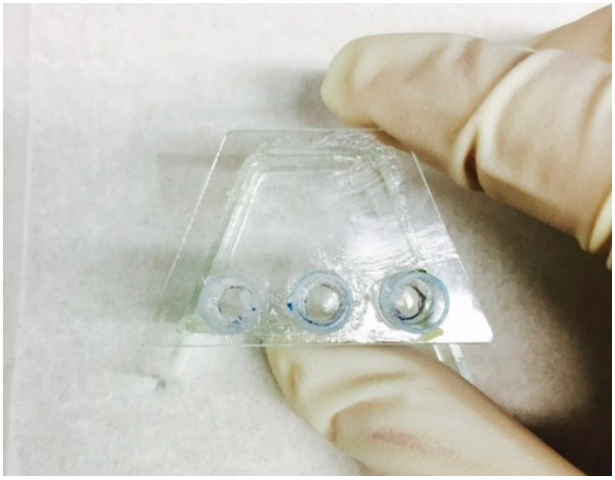

Figure 1.9 An electrochemical cell (cuvette) used for corrosion tests.

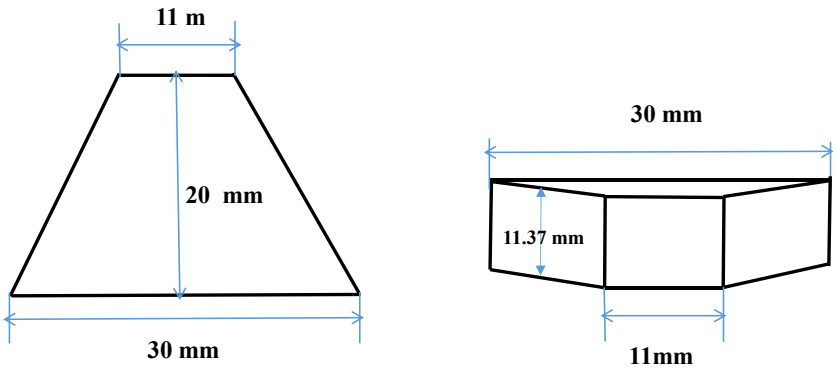

Figure 1.10 A simple sketch in terms of the dimensions of the cuvette.

1.3.2 General Information about In-situ Observations

In order to detect any spatiotemporal changes of our sample surface during pitting events, *in-situ* imaging was adopted with background subtracted contrast enhanced microscope. Optical microscopic techniques are able to produce meaningfully image on an entire area from many hundred μm^2 to several mm^2 *in situ* and in real time, with temporal resolutions limited only by the recording devices used; commercial devices are available with recording rates higher than 1000 frames per second (fps) [40]. These temporal characteristics compensate for the spatial resolution (micron resolution) available to optical techniques. Major components associated with this optical microscope and a schematic diagram are shown in Figure 1.11 and Figure 1.12, respectively. The LED light source and the camera are in two parallel separate paths and are combined using a beam splitter. The lens in front of the aperture assists to focus the light from the LED light source onto the polished surface of the wires. The reflected light beams pass through the lens onto a charge coupled device (CCD) camera sensor. The lateral resolution is approximately 2 μm, which is close to the diffraction limit of the system, and images are recorded at 25 frames per second (fps).

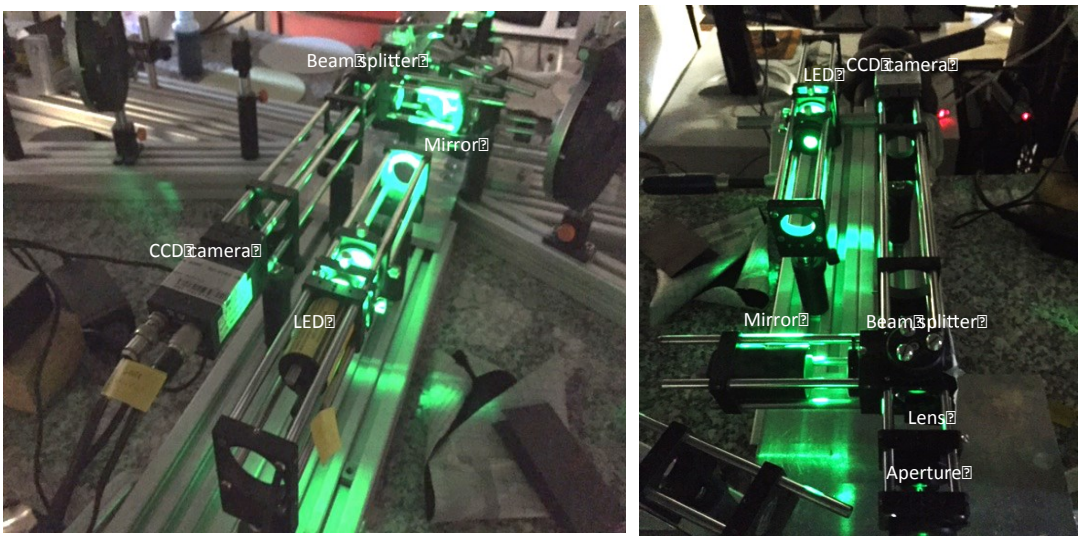

Figure 1.11 Optical microscope with major components labeled. a) A photo take from the backside of the optical set up. b) A view of the microscope from the front side.

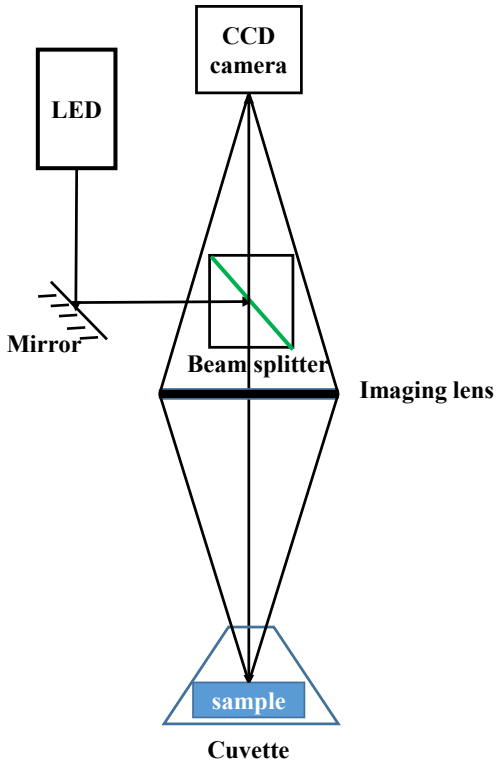

Figure 1.12 A schematic diagram showing the optical microscope.

Due to the limitations of the surfaces smoothness prepared, which did not yield mirror-like surface finishes, ellipsomicroscopy for surface imaging (EMSI) cannot provide much information about the changes of the thickness of the oxide layers on the surfaces during pitting corrosion. The sensitivity of EMSI is on the order of one nanometer or less for detecting changes in layer thickness, despite having lateral resolution only on the order of 10 μm [41].

Initially, a camera flash was fired to synchronize the onset point for both optical microscope and EMSI. A photo detector was used to detect the camera flash. Data was collected with the potentiostat and the CCD camera of the optical microscope, which would be recorded for the same time period after the synchronization process. The electric potential (with respect to the Ag/AgCl electrode) and anodic current data were

plotted versus time as a sequence of graphs updated 25 times per second. In total, two types of the movies can be saved. The first one was associated with each individual sample to provide changes of anodic current on the surface with regards to time sequence during pitting corrosion. Another form of movies were recorded directly by the DVD disc that was connected to the CCD camera of optical microscope, providing in-situ surface observations conveniently. To ensure the synchronization at the end of the in-situ observations, the flash was fired again. The duration of the image recording on CCD camera depended on the scan rate used in the anodic polarization tests conducted with the potentiostat. The background-subtracted sequences allow one to more easily identify pitting sites and subtle changes on the working electrode surface.

1.4 TECHNIQUES USED FOR EX-SITU SURFACE ANALYSIS

1.4.1 Scanning Electron Microscope (SEM)

Scanning electron microscopy (SEM) is one of the powerful surface analysis techniques. It can provide useful information on surface topography, crystalline structure, chemical composition and electrical behaviour of the top 1 μm or so of specimen [42]. The resolution of (SEM) images can reach nm level, and the operational magnifications can be easily adjusted in the range from 10 to 300,000 [43].

During operation of the SEM, the incident electrons are produced from a heated electron gun followed by an accelerating potential (0.1~50 keV) with energies ranging from 2-40 keV [42]. Three typical electron guns are tungsten hairpin filament, Lanthanum hexaboride (LaB_6) filament, and Field emission guns [42]. Accelerated electrons travel through a condenser lens and an electromagnetic field, which raster the

electron beam over the specimen surface. Electrons penetrate the specimen in a teardrop-shaped volume whose overall dimensions are determined by the energy of the electron beam, the atomic masses of elements in the specimen and the angle at which the electron beam hits the specimen [43].

The various interactions between electron beams and specimen produce secondary, backscattered, and Auger electrons [42]. Figure 1.13 below shows the teat-dropped shape specimen interaction volume. Secondary electrons (SE) escape from the specimen with an energy level below 50 eV, resulting from inelastic collisions. . If the vacancy due to the ejection of a SE is filled by an outer shell electron, an X-ray of that energy transition is produced. Most SEs fall in an energy range between 2~5 eV. When the incident electron beams that interact with the nucleus of an atom, elastic events occur. Often, this interaction happens with a change in direction of the beam electrons without a significant change in its energy (<1eV) [43]. If the elastically scattered beam electrons can re-emerge on the specimen surface, the electrons are termed as a backscattered electron (BSE). There are not as numerous as secondary

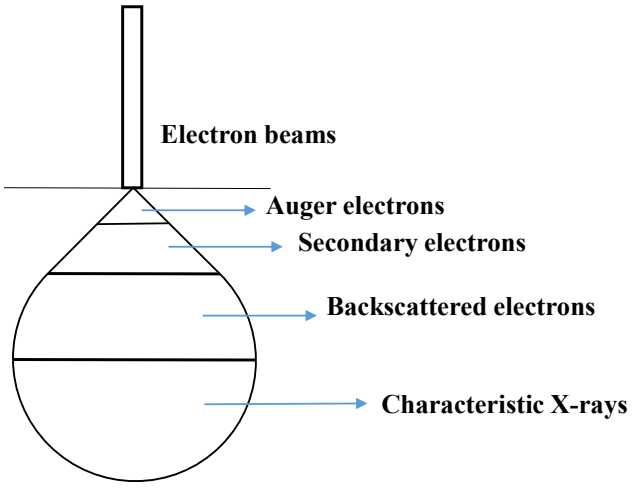

Figure 1.13 A schematic diagram of the major components from electron and specimen interactions of a SEM.

electrons, but they have higher energy. BSEs can have an energy range from 50 eV to nearly the incident beam energy. The fraction of backscattered electrons strongly depends on the atomic number of the scattering atom, which can influence the brightness of an image. Therefore, the intensity of backscattered electrons can be correlated to the atomic number of the element within the sampling volume. The interactions of primary beam and the sample can also lead to the emission of an X-rays due to the fact that shell transitions can happen when outer-shell electrons fill a vacancy in the inner shell of an atom. The emitted X-ray has an energy characteristic of the parent element. Measurements and the energy of the emitted X-rays allow the chemical and elemental analysis, which is often used in energy dispersive X-ray Spectroscopy. This is a technique that is normally coupled with SEM surface analysis.

In our work, the detection was performed by using a HITACHI S-4700 SEM machine to observe the sample surfaces before and after corrosion.

1.4.2 Energy Dispersive X-ray Spectroscopy (EDS)

The surface analysis performed on backscatter electrons (BES) display compositional contrast that results from different atomic number elements and their distribution [44]. Energy Dispersive Spectroscopy (EDS) allows one to identify what those particular elements are and obtain compositional information of various elements (Atomic % for example).

Energy-dispersive X-ray spectroscopy (EDS, EDX, or XEDS), sometimes called as energy dispersive X-ray analysis or energy dispersive X-ray microanalysis (EDXMA), is an surface analytical technique used for the elemental analysis or chemical characterization of a sample [45]. EDS analysis often relies on the fact that

each element has a unique atomic structure allowing unique set of peaks on its X-ray emission spectrum. The excitation caused by the incident beam leads to the ejection of an electron from an inner shell, while creating an electron hole where the electron was. An electron from an outer, higher-energy shell then fills the hole. The difference in energy between the higher-energy shell and the lower energy shell may be released in the form of an X-ray [44]. As the energies of the X-rays are characteristic of the difference in energy between the two shells and of the atomic structure of the emitting element, EDS allows the elemental composition of the specimen to be measured.

In this work, EDS analysis was also carried out with the same machine as SEM, which is the HITACHI S-4700 microscope.

1.4.3 Atomic Force Microscopy (AFM)

Atomic Force Microscopy (AFM) which can be operated in air or water, uses a fine tip (apex radius ~10 nm) to map surface morphology and mechanical and chemical properties through an interaction between the tip and surface [46]. The demonstrated resolution is on the order of fractions of a nanometer.

The AFM consists of a cantilever with a sharp tip (probe) at its end, which is used to scan the specimen surface. The cantilever is typically silicon or silicon nitride with a tip radius of curvature on the order of nanometers. When the tip is brought along the sample surface, forces between the tip and the sample lead to a deflection of the cantilever according to Hooke's law [47]. The spring constant is one of the critical components for a cantilever. The resonant frequency f_0, of the spring system is given by the equation below,

$$f_0 = \frac{1}{2\pi}\left(\frac{k}{m_0}\right)^{1/2} \qquad (1.1)$$

Where k is the spring constant, and m_0 is the effective mass that loads the spring. The equation implies that as we decrease the k to soften the spring, m_0 should also be deceased to keep the ratio of k and m_0 large. This consideration is based on the fact that the maximum deflection of a given force is required for a better surface analysis, which suggested that the spring should be soft enough [47].

This deflection can be detected by a laser focused on the back of the cantilever. The laser is reflected by the cantilever onto a distant photodetector. The movement of the laser spot on the photodetector provides the measurement of the movement of the probe. This set-up is known as an optical lever. The probe is moved over the sample by a scanner, typically a piezoelectric element, which can make extremely precise movements with angstrom accuracy. The combination of the sharp tip, the very sensitive optical lever, and the highly precise movements by the scanner, combined with the careful control of probe-sample forces allow the extremely high resolution of AFM. The configuration of AFM is shown in Figure 1.14 below.

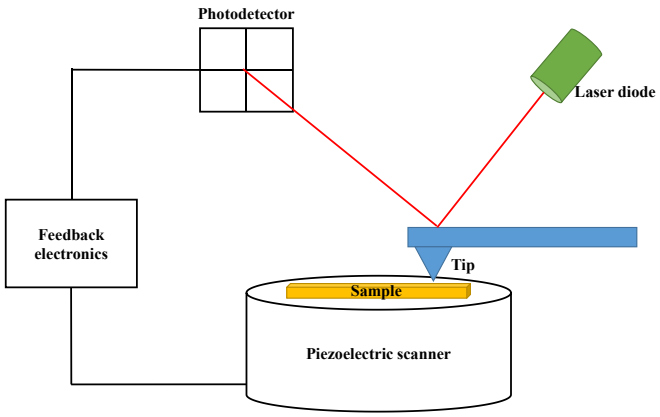

Figure 1.14 Schematic of AFM operation.

AFM operation is usually described as one of three modes, which are contact mode, tapping mode and noncontact mode. Contact mode is often called a static mode, and Tapping and noncontact are called dynamic modes, as the cantilever is under oscillation. Typically, this is done by adding an extra piezoelectric element that oscillates up and down at somewhere between 5-400 kHz to the cantilever holder [46]. The main difference lies in between tapping mode and noncontact mode is that in tapping mode, the tip of the probe actually touches the sample, and moves completely away from the sample surfaces in each oscillation cycle. However, in noncontact mode, the cantilever stays close to the sample all the times, and has a much smaller oscillation amplitude.

AFM has been applied to a wide range of disciplines of the natural sciences, including solid state physics, semiconductor science and technology, polymer chemistry and physics, surface chemistry, molecular biology, cell biology and medicine.

In our work, A Keysight 5500 AFM instrument was also used to characterize the surface roughness before and after corrosion.

1.4.4 X-ray Photoelectron Spectroscopy (XPS)

X-ray photoelectron spectroscopy (XPS), is a surface analytical technique that depends upon the measurement of the energies of photoelectrons that are emitted from atoms when they are irradiated by soft X-ray photons (1 – 2 keV) [48]. XPS spectra are obtained by irradiating a material with a beam of X-rays while simultaneously measuring the kinetic energy and number of electrons that escape from the top 0 to 10

nm of the material being analyzed. Ultra-high vacuum (UHV) condition (Pressure is lesser than 10^{-9} millibar) is required for the operation of XPS.

XPS was first developed in the mid-1960s by K. Siegbahn and his research group. K. Siegbahn was awarded the Nobel Prize for Physics in 1981 for his work in XPS [48]. The basic principle of XPS is based on the photoelectric effect described by Einstein in 1905 where the concept of the photon was used to describe the ejection of electrons from a surface when photons impinge upon it. Al Kalpha (1486.6eV) or Mg Kalpha (1253.6eV) are often used as the monochromatic X-ray sources in XPS analysis. By the conservation of energy, the binding energy (BE) of the ejected electrons from a specific elemental atom can be determined by the kinetic energy (KE) measured in XPS analysis. Figure 1.15 shows a simple diagram that a photoemission process is involved for XPS surface analysis.

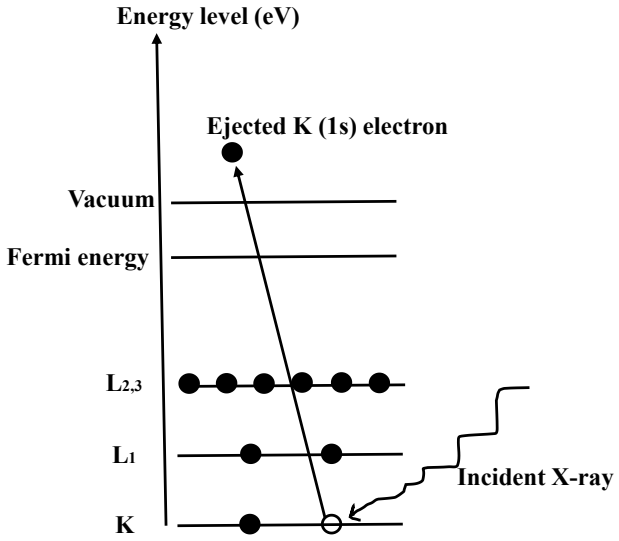

Figure 1.15 A diagram shows photoemission process involved for XPS surface analysis.

The relationship between BE and KE is shown in the equation below by following Koopman's theorem [48]:

$$KE = h\nu - BE \qquad (1.2)$$

, where h is the Plank's constant and υ is the frequency of a photon. Equation 1.2 was furthered developed into equation 1.3 so as to take into account the work function (φ) of a solid material, which is shown as below.

$$KE = h\nu - BE - \varphi \qquad (1.3)$$

The energy of the photoelectrons leaving the sample are determined using a Concentric Hemispherical Analyzer (CHA). It gives a spectrum with a series of photoelectron peaks. The BE of the peaks are characteristic of each element [49]. The peak areas can be used to determine the composition of the materials surface. The shape of each peak and the BE can be slightly altered by the chemical state of the emitting atom. Therefore, XPS can provide information of chemical bonding as well. A typical XPS spectrum is a plot of the number of electrons detected (sometimes per unit time) (Y-axis, ordinate) versus the binding energy of the electrons detected (X-axis, abscissa). Each element produces a characteristic set of XPS peaks at characteristic binding energy values that directly identify each element that exists in or on the surface of the material.

Besides the production of characteristic X-rays for the core hole, another possible phenomenon is related to ejection of Auger electrons. The emission that associates with Auger electron for the core hole is illustrated in the Figure 1.16 below.

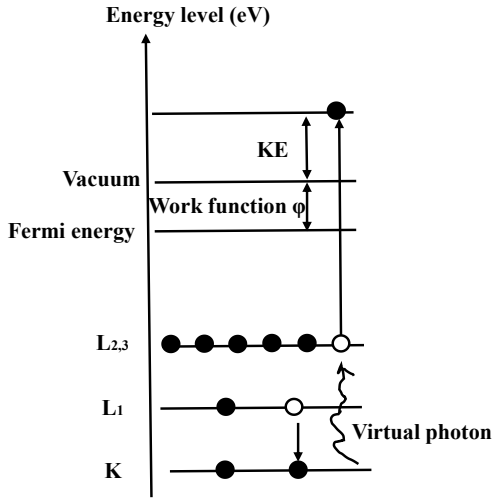

Figure 1.16 An emission of an Auger electron.

As can be seen from Figure 1.16, the core hole can be filled by an outer shell electron, whereby the electron moving to the lower energy level loses an amount of energy equal to the difference in orbital energies, which is considered to be a virtual photon. This energy can be coupled to a second outer shell electron, which will be emitted from the atom if the transferred energy is greater than the orbital binding energy [48]. The Kinetic energy of the emitted Auger electron is shown in the equation 1.4 below:

$$\mathrm{KE} = \mathrm{E_{core}} - \mathrm{E_1} - \mathrm{E_2} \quad (1.4)$$

, where E_{core}, E_1 and E_2 are the core level, first outer shell, and second outer shell electron energies, respectively. The escape depth of electrons is localized to within a few nanometers of the sample surface, giving Auger electron spectroscopy (AES) an extreme sensitivity to surface species [48]. Because of the low energy of Auger electrons, most AES setups are run under ultra-high vacuum (UHV) conditions. Such measures prevent electron scattering off of residual gas atoms as well as the formation

of a thin "gas (adsorbate) layer" on the surface of the specimen, which may degrade analytical performance [48].

The relationship between the yield of x-rays and Auger electrons is illustrated in Figure 1.17 below. The yield per K shell vacancy of Auger is decreasing with an increase in the atomic number, whereas an increasing trend that is related to X-ray yield can be observed simultaneously [50].

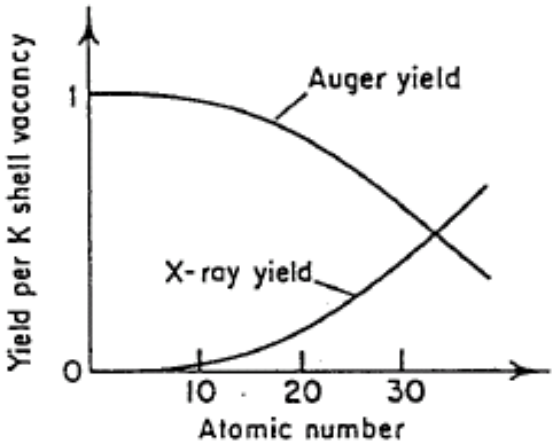

Figure 1.17 Yield per K shell vacancy of both Auger and X-ray is plotted as function of atomic number.

In this work, X-ray photoelectron spectroscopy (XPS) analysis was carried out using a Kratos Axis Ultra spectrometer using a monochromatic Al Ka source (15 mA, 14 kV) to measure the elemental composition and different compounds of the passive layers formed on the surface before and after corrosion.

1.5 BRIEF REVIEW OF HETEROGENEOUS WETTING

1.5.1 Surface Tension and Contact Angle—Young's Equation

Wettability of a solid surface depends on the surface free energy of the substrate [51]. If considering a liquid droplet on a flat horizontal surface, the contact angle of the droplet is defined as the angle formed by the intersection of the liquid-solid interface and the liquid-vapor interface [52], which can be geometrically obtained by creating a tangent line from the contact point of liquid and vapor interface. Small contact angles (< 90°) correspond to high wettability, while large contact angles (> 90°) correspond to low wettability. Figure 1.18 illustrates three contacting mode of a liquid droplet mentioned above [52].

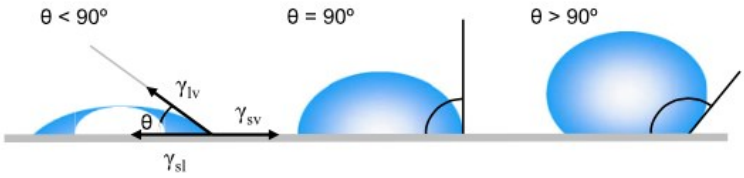

Figure 1.18 An illustrations of contact angles formed by a liquid drop formed on a flat homogeneous solid surface [43].

As can be seen from Figure 1.18, θ is the contact angle; γ_{sv}, γ_{sl} and γ_{lv} are the surface tension of solid/vapor, solid/liquid, and liquid/vapor interfaces, respectively. Droplet with smaller contact angle (θ< 90°) is widely spread on the solid surfaces, indicating the wetting of the interface is favorable, whereas liquid drop with larger contact angle (θ > 90°) has a relatively smaller contact area on the surface. For super-

hydrophobic surfaces, water contact angles are usually greater than 150°, showing almost no contact between the liquid drop and the surface [51].

The relationship of surface tensions and contact angle of a liquid drop on an ideal solid surface was first described by Thomas Young [53], which stated that the mechanical equilibrium of the droplet under the action of three interfacial tensions (γ_{SV}, γ_{SL} and γ_{LV}. This is called Young's equation:

$$\gamma_{lv} \cos\theta = \gamma_{sv} - \gamma_{sl} \qquad (1.5)$$

Generally speaking, the shape of a liquid droplet is determined by the surface tension of the liquid. In a pure liquid, forces exerted on each molecule in the bulk equally balanced in every direction due to the interaction with neighboring liquid molecules, resulting in a net force of zero. However, part of the molecules exposed at the surface of the droplet does not have neighboring molecules in all directions, thus, resulting in an unbalanced force system. To be specific, they are pulled inward by the neighboring molecules below and an internal pressure is created. Consequently, the liquid spontaneously contracts its surface area to maintain the lowest surface free energy.

In our research, a plausible description accounts for the fact of the improvement of corrosion resistance on patterned samples, can be attributed to heterogeneous wetting approach [54]. This type of wetting model depicts the fact that surfaces under the droplet of the samples are filled up with air molecules, which act as a barrier to prevent the sample surface from the direct contact with corrosive electrolyte. The reasoning depends on two major factors, which are relatively high surface roughness and low surface energy. A droplet of water on a relatively rough surface with low

surface energy can be demonstrated with two possible contact modes: Wenzel and Cassie modes [55]. Figure 1.19 depicted Wenzel and Cassie model.

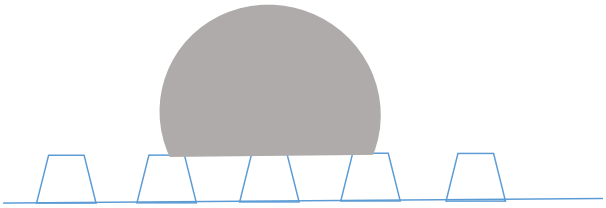

(a)

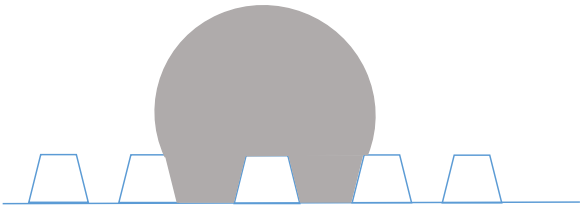

(b)

Figure 1.19 An illustration of two different models of the wetting behavior of a liquid droplet. a) Cassie model with vapor pocket as a barrier as against corrosive electrolyte. b) Wenzel model with no air intrusion between liquid drop and substrate.

In the model of Wenzel [56], there is no possible air pathway between the liquid droplet and the surface itself. Equation 1.6 describes this phenomenon:

$$\gamma_{lv} \cos \theta_w = r(\gamma_{sv} - \gamma_{sl}) \qquad (1.6)$$

Combination of equation1.5 and 1.6 yields equation 1.7:

$$\cos \theta_w = r \cos \theta, \qquad (1.7)$$

where θ_w is the apparent contact angle, r is the factor of surface roughness and θ is the intrinsic contact angle [47].

In the theory of Cassie [57], vapor pockets are assumed to be trapped underneath the liquid, which provides a composite surface, in which θ_c can be expressed by chemical heterogeneity of a rough surface in equation 1.8:

$$\cos \theta_c = f_s \cos \theta_s + f_v \cos \theta_v \qquad (1.8)$$

θ_c is the apparent contact angle in the Cassie mode; θ_v and θ_s are the intrinsic contact angles of water to the solid and vapor, respectively. f_S and f_V are the area fractions of solid and vapor on the surface.

Based on all the information provided above, model of Cassie theory could be considered as the reason for the enhancement of corrosion resistance of the samples. Transitions between Cassie's and Wenzel's states have been reported [55], which could indicate the fact that some of the patterned samples do not exhibit a better corrosion performance with the same corrosive electrolyte. This part of the study with regards to the transitions between two models could be a possible route for future research work. Chapter 3 demonstrated the work done in the second project.

CHAPTER 2 THE EFFECT OF SURFACE MORPHOLOGY ON CORROSION

The Effect of Surface Morphology on Corrosion Performance of SS 316LVM Biomedical Devices

Authors: Alisina Toloei, Mengnan Guo, and Harm. H. Rotermund.

Department of Physics and Atmospheric Science, Dalhousie University, 6310 Coburg Road, Halifax, Nova Scotia, B3H 3J5, Canada.

Journal of Materials Engineering and Performance, 2015, Volume 24, Issue 10, pp 3726-3736

All figures, texts were contributed by Mengnan Guo. Alisina Toloei and Harm H. Rotermund contributed editing and modification.

2.1 ABSTRACT

In this study, in order to investigate the relationship between surface roughness and the corrosion resistance of the SS 316 LVM wires, samples have been prepared with different surface roughness by using different grits of SiC papers. In order to simulate the environment of implanted biomedical devices, a three-electrode electrochemical cell with 0.9% (by mass) NaCl solution has been used to test the corrosion resistance of the samples by potentiodynamic method and anodic polarization tests. SEM, EDS, and XPS have been per- formed to analyze the surfaces appearance and chemical elements on the surface before and after the corrosion. AFM was also

used to get 3D images of the surface and to show the change in roughness of the samples after corrosion testing. Background-subtracted contrast-enhanced microscopy has been performed *in situ* to detect the pitting process happening on the surface of stainless steel samples. It was concluded that a relatively smooth surface could result in higher corrosion resistance and larger potential of stable pitting, whereas a rough surface can easily go into stable pitting with lower pitting potentials. Rougher surfaces also showed a shorter time for the formation of stable pits. Microscopy observations illustrated more corrosion on rougher surfaces, and EDS showed more chloride ion remained on these surfaces.

2.2 INTRODUCTION

Pitting corrosion is one of the most widespread and dangerous forms of localized corrosion of passive metals, which commonly occurs in a range of aggressive environments, and the most common type of aggressive ions is chloride ion found in many natural and industrial environments [58]. The corrosion resistance of stainless steel (SS) originates from the protective oxide film, which spontaneously forms on the surface of the metal and acts as a barrier against aggressive diffusion of ions into the metal itself [29], which often attacks the disruptions located on the surface of the passive layer. These disruptions include grain boundaries, scratches, and surface stoichiometric inhomogeneity, which appeared to concentrate pit onsets significantly [59].

There are a number of methods related with the prevention of corrosion and pitting corrosion on passive metals [60]. The first one is by alloying the original

material, with another element, i.e., molybdenum is more effective in increasing the pitting corrosion resistance [6,7,60]. A second strategy to enhance the corrosion resistance is use of various types of coatings [60,61]. Other prevention methods can be achieved by altering the structural composition of the metal materials, such as annealing at higher temperatures [62]. In addition to these three typical prevention methods, surface modification is emerging as another promising way to assist in the process of enhancement of corrosion resistance of passive metals [63]. This is mentioned to be a vital part for the bio-implantations inside the human body. For instance, Liang et al. modified the surface of AISI 304 stainless steel by the plasma nitriding, which showed the lowest current density and the most positive breakdown potential [64]. Lim et al. adopted the method of laser shock peening to perform the enhancement of abrasion and corrosion resistance of duplex stainless steel, which revealed that the corrosion rate of duplex stainless steel can be reduced as much as 74.2% [35]. Klages et al. modified the surface of the stainless steel 316LVM by high-purity deionized water for different time durations, which showed the greatest enhancement of pitting resistance when tested in 0.9% (by mass) NaCl solutions [29].

Surface roughness of active-passive metals is also reported to affect corrosion performance [54,65–69]. An active-passive metal can first undergo passivation due to the formation of passive oxide layers with almost no change in current density, which is said to be undergoing an active /passive transition [3]. However, it can be active again if the a large potential is added to the metal which falls in the trans-passive region, where an increase in current density can be observed with an increase in potential [3]. A smoother surface assists to decrease the frequency of metastable pitting because of

less number of metastable pitting sites available [66]. GT Burstein at et al. examined the corrosion resistance of stainless steel 304 with different surface roughness in 1 M NaCl solution [66]. It was shown that the pitting potential of a relatively smoother surface is higher than that of a rougher one. Hong at el. performed AC impedance measurements on type 301 stainless steel, which is wet-ground on silicon carbide papers ranged from 240 to 1500 grits [70]. The results showed the breakdown potential increased with the decrease of surface roughness. Sasaki and Bursten showed that increasing the roughness lowers the pitting potential in chloride solution [65]. J. Beddoes and K. Bucci determined the susceptibility to pitting and crevice corrosion in 316L samples prepared according to industrial practices for bone fixture plates which showed that electropolished surfaces provide the best resistance to crevice corrosion [71] , while bead-blasted surfaces provide the best resistance to pitting corrosion. Cisse et al. showed the effect of surface treatment of NiTi alloy on its corrosion behavior in simulated body condition, which reported that the electropolishing sample exhibits no susceptibility to localized corrosion when placed in a living body [72].

Kaczmarek et al. presented the electrochemical behavior of NiTi alloy [73]. The results clearly showed that surface treatment can be viable for medical implants due to the increase of the corrosion resistance. The relationship between corrosion and surface roughness has been investigated for aluminum alloys, copper, titanium, and magnesium alloys [74–77]. In all cases, by decreasing the surface roughness, both the general corrosion rate and pitting degradation decreased. However, to the authors' best knowledge, there is no published data on the effect of surface roughness on the corrosion behavior of SS 316 LVM in 0.9% (by mass) NaCl solution.

In this study, potentiodynamic method and anodic polarization tests were used to investigate the effects of different surface roughness on pitting potential, time of the initiation of stable pitting, and average peak values of corrosion current. Contrast-enhanced microscopy and SEM have been used for the first time to visualize the pits and severity of corrosion on the surface of stainless steel samples. AFM was used to monitor the change in roughness of samples after corrosion. EDS also compared the elements on the surface before and after corrosion.

2.3 EXPERIMENTAL PROCEDURES

2.3.1 Materials Preparation

In this work, the samples used were low-carbon stainless steel (SS 316 LVM wires), which were 0.381 mm (0.015 in.) in diameter (Smallparts Inc.) In the mechanical polishing process, all of the wires were hold by the sample holder mounted by the Crystalbond adhesive. Five different types of wires have been ground by incrementally finer SiC papers (G120, G240, G600, G1200, and G1500). The direction of the sample holders was turned by 90° against its original direction when moving to a finer SiC paper to remove the unidirectional roughness from the previous step. All of the samples underwent mechanical polishing and cleaning by high-purity deionized water (18 MΩ/cm Nanopure) before the start of the experiments. Microscopic inspections were performed to ensure no visible particles were left on the face of the wires. In order to simulate the environment of implanted biomedical devices, 0.9% (by mass) NaCl solution was used to test the corrosion resistance of the wires. The stainless steel wires were then bent so they could be inserted into the access ports on the top of

the cuvette (solution container) and finally were painted for three times with a clear lacquer under a stereomicroscope so that only the face of the wire with unidirectional roughness remained uncoated. All wires were kept for 30 min until the nail polish dried out, and then inserted into the cuvette containing NaCl solution for the duration of 30 min before starting the corrosion tests. Details of the experimental setup are shown in Fig. 2.1. The LED light source and the camera are in two separate paths and are combined using a beam splitter before the lens. The lens assists to focus the light from the LED light source onto the polished face of the wire and the reflected light pass through the lens onto a CCD sensor. The lateral resolution is approximately 2 μm, which is close to the diffraction limit of the system, and images are recorded at 25 fps. Klages et al. and Dornhege et al. used the same apparatus to investigate pitting corrosion of stainless steel 316 LVM [31,78].

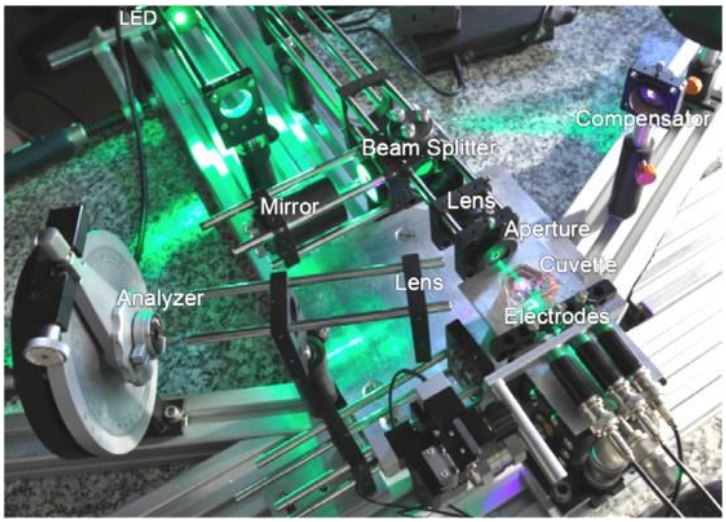

Figure 2.1 A photo of the aligned experimental setup includes optical microscopy and corrosion cell.

2.3.2 Instruments

A three-electrode system was used in the electrochemical tests. An Ag/AgCl wire was used as the reference electrode, a Pt wire served as the counter electrode, and the polished stainless steel wire face used as the working electrode. The potentiostat used to do the corrosion testing was a Fritz-Haber-Institute, Berlin-ELAB-G050-29 model. The whole area of the wires (except the polished face) was insulated from the solution by nail polish. Before starting the scanning, all the samples have been immersed in the NaCl solution for 30 min to stabilize the sample. The potential was first scanned from -600 mV with respect to the Ag/AgCl electrode to 0 mV. It has been increased in steps of 100 mV at a rate of 10 mV/s after 0 mV and held at each step for 1 min. The potential was then reversed when a significant increase in current was detected. The anodic polarization tests associated with non-stop tests were performed until reaching the stable pitting that the potential has been reversed to its initial value of -600 mV. The potential was increased to a minimum of 800 mV. In order to observe the stable pitting, the potential was continuously increased if no pitting events could be observed at 800 mV. To verify the pitting events occurred on the polished face, *in situ* optical techniques were employed. Background- subtracted contrast-enhanced microscopy has been performed to visualize the pitting process during corrosion testing.

The SEM used was a HITACHI S-4700 microscope to see the appearance of the surfaces before and after corrosion. EDS was also carried out with the same machine. X-ray photoelectron spectroscopy (XPS) analysis was carried out using a Kratos Axis Ultra spectrometer using a monochromatic Al Kα source (15 mA, 14 kV)

to measure the elemental composition and different compounds on the surface. A Keysight 5500 AFM instrument was also used to characterize the surface roughness before and after corrosion.

2.4 RESULTS AND DISCUSSION

2.4.1 Corrosion Testing

Table 2.1 shows the average corrosion current and potential values from corrosion testing for samples with different surface roughness. As it is seen, by decreasing the roughness from sample G120 to G1500, the pitting potential for both stop and non-stop tests shifted to more positive values indicating an earlier onset of pitting for rougher surfaces. Corrosion current showed higher values for rougher surfaces indicates increased corrosion rate on these samples. Stable pitting also occurred in a shorter time for rougher samples compared to smoother ones. The pitting potential is the potential where the onset of pitting starts. Samples that requires a high pitting potential are considered to be more corrosion resistant. The critical current is the largest current response after the initiation of pitting. In our work, it is considered that a relatively higher current response can be indicative of a more intense corrosion event on the sample surface.

Figure 2.2 (a)-(d) shows the wire surface at the beginning and the end of corrosion tests of samples G 240 and G 1200 as examples of a rough and a smooth surface. Generally, by decreasing the roughness, the brightness of surface increased because of the better reflection of light off the wire surface. As can be seen in Figure 2.2 (a) and (b), some black dots are seen in the center and also on the left side of Fig. 2.2 (b) which are corrosion pits, whereas from Figure 2.2 (c) and (d), no significant

change can be observed from the surface of sample G 1200 during and at the end of the corrosion test, indicating a lower degree of the pitting corrosion on the smoother surface. Furthermore, as reported by researchers, most of the corrosion that happened on the rough surface is along the grooves [79].

Table 2.1 Corrosion parameters for samples with different surface roughness.

Sample	$E_{pit(non-stop)}$ /V	$E_{pit(stop)}$ /V	$I_{Critical}$/ μ A	Time of stable pitting/s
G120	0.83	0.84	31.20	640.7
G240	1.01	1.02	30.78	802.6
G600	1.09	1.23	12.96	851.0
G1200	1.14	1.28	9.03	883.9
G1500	1.22	1.29	8.47	929.0

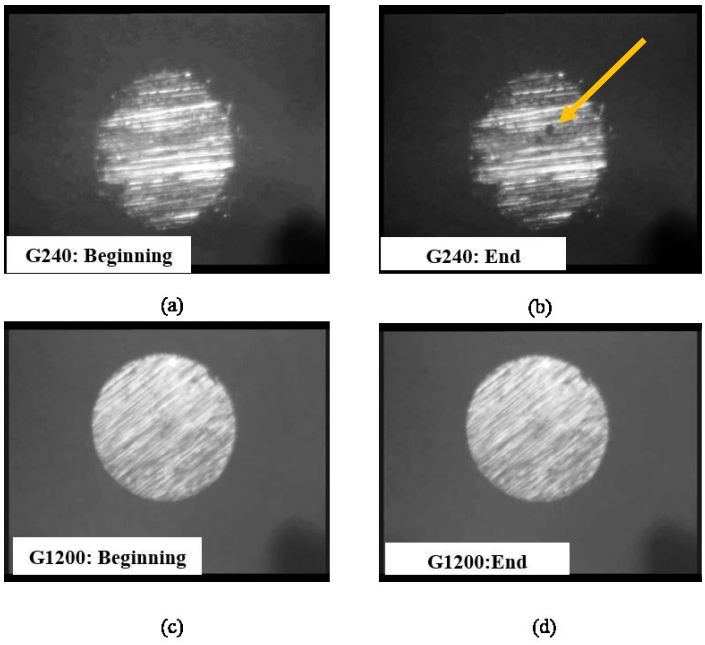

Figure 2.2 *In situ* observation of background-subtracted contrast-enhanced microscopy for samples G 240 (a) and (b) and G1200 (c) and (d).

The potentiodynamic test results are presented in Figure 2.3 (a)-(e). The plots illustrate the potential and current values versus time for five wires with different surface roughness. The average time related to the initiation of stable pitting, the potential, and the current values on different samples are listed in Table 2.1. By decreasing the roughness from sample G120 to G1500, samples showed more resistance against corrosive solution and the dramatic increase in current happened in a later time (ranged from 600 s to around 900 s). The earliest metastable pitting was indicated by an anodic spike at 100, 500, 100, 250, and 150 mV for samples G120, G240, G600, G1200, and G1500, respectively. The number of metastable events, shown by smaller anodic spikes (current lower than 1 μA), which happened before the stable pitting, had a decreasing trend by the decrease of surface roughness. This phenomenon has been reported by Burstein and Pistorius [66]. The pitting potential increases with the degree of smoothness of the surface. In our experiments, the pitting potential increased from 840 to 1300 mV as the surfaces of the wires got smoother. This result indicated that enhancement of corrosion resistance can be achieved by decreasing the surface roughness for active-passive metals. This is in agreement with other researches [70,79], where it has been demonstrated that smooth surfaces increase corrosion resistance, while rough surfaces are less resistant. A similar behavior was reported by [74] for Cu in a 3.5% NaCl solution.

If the pitting potential of all samples is considered at a specific current value (Figure 2.3), it can be seen that in the sample with lowest roughness (G1500), the onset of pitting is shifted to higher potential [76]. The breakdown of the protective film

begins at the point which is known as critical pitting or breakdown potential. This is where the likelihood of pitting is the greatest and the point is used as a parameter for assessing pitting properties of the tested materials. This point happens at higher potential values for surfaces with lower roughness values

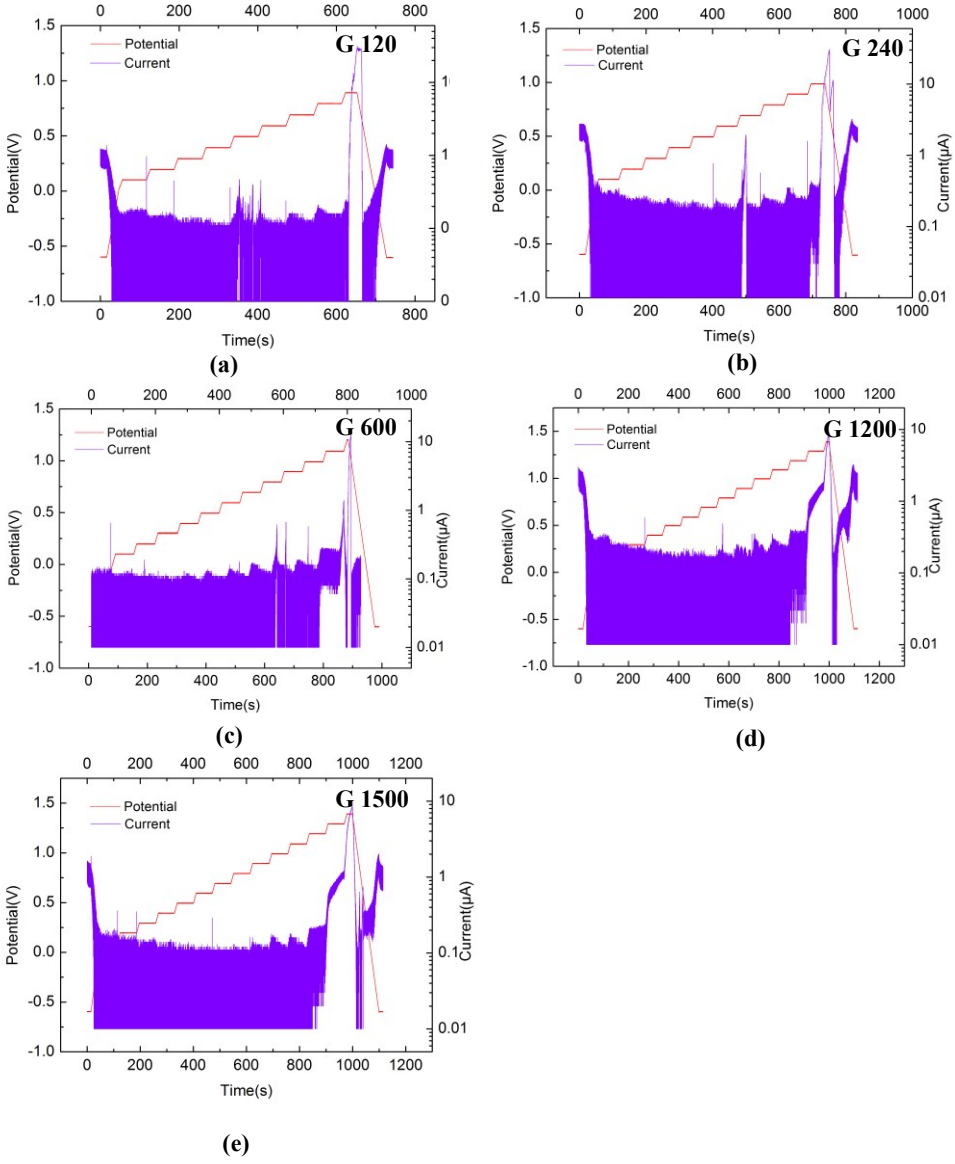

Figure 2.3 Plots of potential and current vs. time for five wires with different surface finish.

Figure 2.4 shows the single current versus time plots for different surface roughness. By decreasing the roughness, the maximum anodic pitting current gradually decreased, which suggested that the smoother surface has higher corrosion resistance compared to rougher ones. A similar trend in polarization resistance vs. unidirectional roughness has been reported by Lee and Lee for 21 Cr ferritic stainless steel in a 1 M NaCl solution [80].

The corrosion results clearly showed that an increase in surface roughness leads to a decrease in pitting potential, and therefore an increase in corrosion current. In the rougher samples, there is more contact area between the corrosive solution and the substrate. There is also trapping of the corrosive ions including chloride in the deep grooves, resulting in an autocatalytic process such as pitting [41]. Both of these factors would lead to an increased corrosion rate. The trend is consistent with the research of Li and Li who measured the electron work function of Cu and found that a rougher surface could more readily release electrons that would result in a higher corrosion [74].

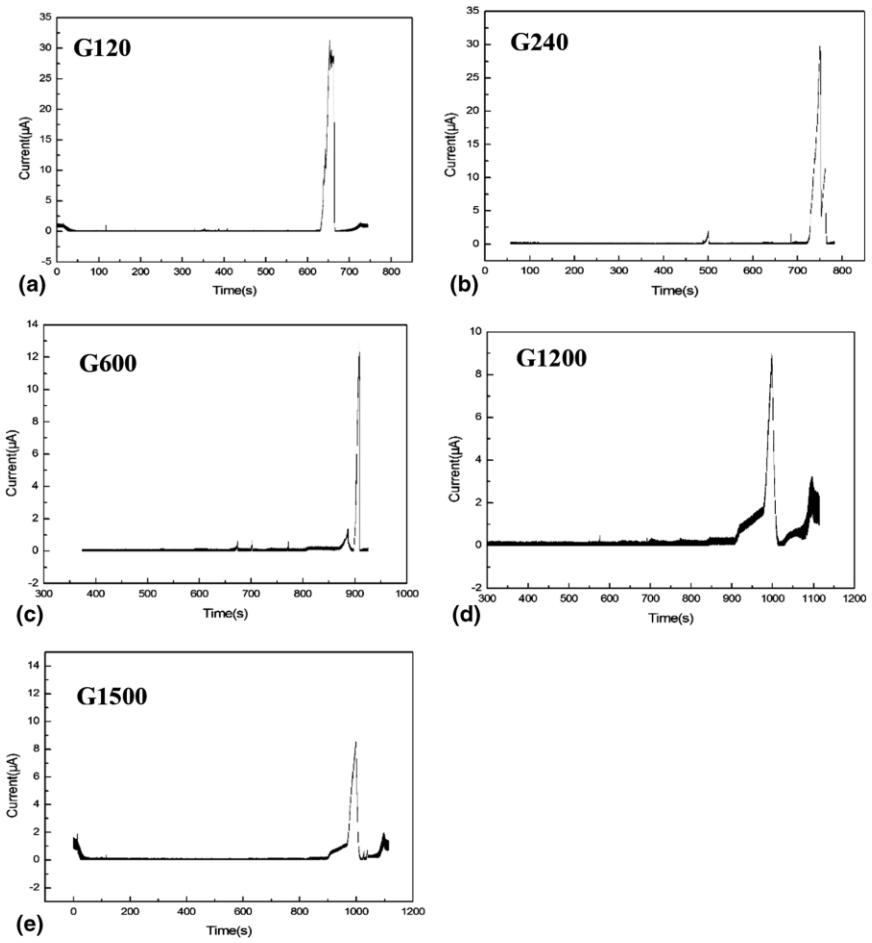

Figure 2.4 Current vs. time for wires with different surface finish.

2.4.2 SEM

Figure 2.5 presents SEM micrographs of two of the samples (G240 and G1200) with unidirectional roughness as representatives of rough and smooth surfaces both before and after corrosion, respectively. According to Figure 2.5 (a) and (b), we can see that for the rougher surface, severe corrosion can be seen in different parts and corrosion taken place over the total sample surface. By decreasing the roughness in Figure 2.5(c) and (d), the grooves are not as obvious as before corrosion and no

significant corrosion can be seen on the surface except some small corrosion products. The observations are in agreement with the observations of Toloei and Suter that deeper grooves trap the corrosive ions and corrosion products and will result in more corrosion. The results also confirm corrosion results and *in situ* observations [69,76].

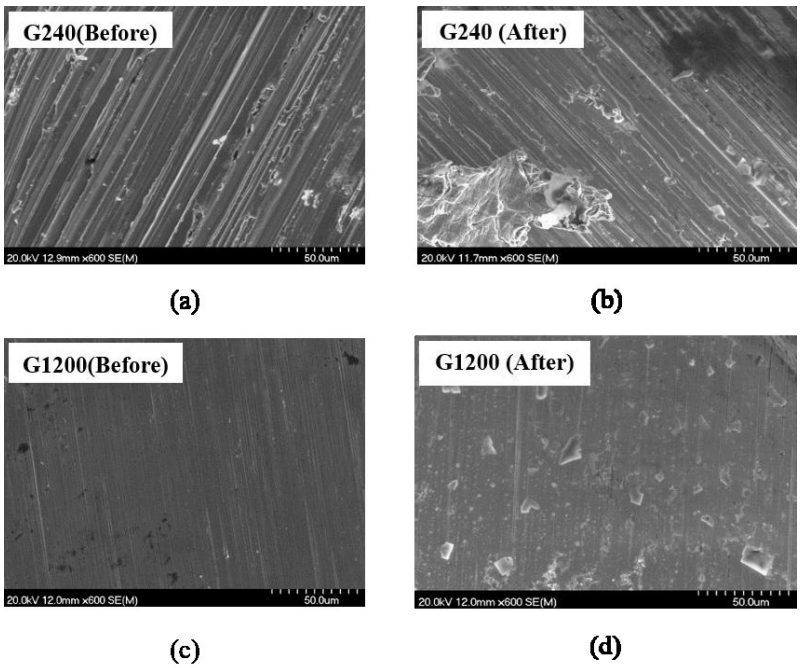

Figure 2.5 SEM micrograph of SS samples G240 (a) and (b) and G1200 (c) and (d) before and after corrosion.

2.4.3 EDS

EDS measured the change in different elements weight percent including oxygen and chlorine on the surface of the samples before and after corrosion testing, and the results are summarized in Table 2.2. Figure 2.6 also shows the EDS spectra showing different elements on the surface of samples G240 and G1200 before and after corrosion. All samples had low oxygen contents before corrosion testing but the oxygen content increased for all samples after corrosion. Looking at the oxygen content

increase of the surface, the largest increase was for the roughest sample (G120). For the smoother samples in Table 2.2 (G600-G1500), the increase in oxygen content was not significant. As demonstrated from the electrochemical results, sample G120, which showed the highest increase in oxygen content, exhibited the highest corrosion current and the lowest potential. For smoother samples, this increase in oxygen content could be indicative of the formation of a stable passive film, as suggested by Suter for high-purity aluminum, and for rougher surfaces, more oxygen is related to corrosion products and oxide layer [76]. As it is seen, there is no chlorine before corrosion and after corrosion more chlorine was found on rougher surfaces. This phenomenon confirms our justification for more corrosion on these surfaces because of trapping of corrosive ions on rougher surfaces, which is in agreement with previous studies [69,76].

Table 2.2 EDS analysis before and after corrosion of five types of samples.

Weight percentage \ Sample	G120	G240	G600	G1200	G1500
Oxygen content (Before)	0.48	0.59	0.86	1.23	0.73
Oxygen content (After)	13.06	4.71	1.81	1.85	1.90
Cl content (Before)	0	0	0	0	0
Cl content (After)	2.26	1.41	0.72	0.50	0.22
Change in oxygen content	12.58	4.12	0.95	0.62	1.17
Change in Cl content	2.26	1.41	0.72	0.50	0.22

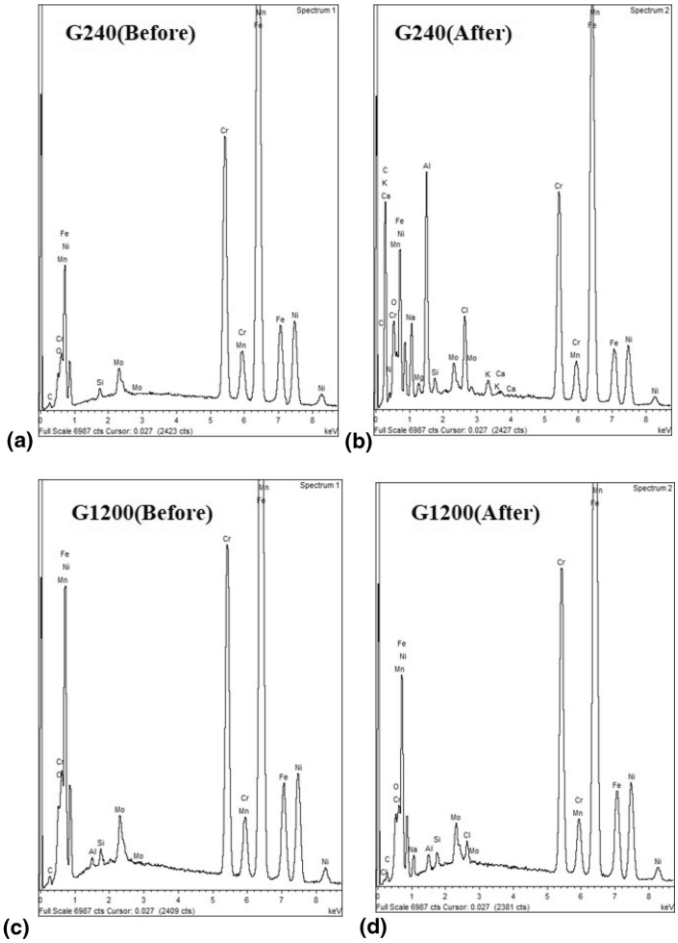

Figure 2.6 EDS spectra for samples G240 (a) and (b) and G1200 (c) and (d) before and after corrosion.

2.4.4 XPS

Table 2.3 Significant elements on the surface before and after corrosion as determined by XPS.

Percentage Atomic Concentration	G 240	G 1200
O (Before)	32	21.8
O (After)	23	29.7
Cr (Before)	2.2	2.3
Cr (After)	1.2	2.1
Cl (Before)	0	0
Cl (After)	2.4	2.1
Fe(Before)	5	3
Fe(After)	1.5	3.3

A comprehensive XPS study in terms of the passive layers that were formed before and after corrosion on samples with different roughness was performed. The results for sample G240 and G1200 are presented as examples of a rough and a smooth surface. Table 2.3 shows percentage atomic concentration (at. %) of different elements presented on the surface for samples G240 and G1200 before and after corrosion. As can be seen, sample G240 had more oxygen before corrosion and it is because of higher roughness and more contact area on the surface. But after corrosion, more oxygen was found on sample G1200 (the smoother sample) that is related to the formation of the passive layer. Chromium also shows a higher value on sample G1200 after corrosion (helping the formation of chromium oxide). More Fe on G1200 after corrosion also can be attributed to more iron oxide. The existence of chloride ions can be related to contaminants deposited on the surface after corrosion. This results are in great agreement with EDS results, indicating that less Cl^- ions were found on samples with

smooth surface finishes than that on the rougher ones. More oxygen was found on smoother samples after corrosion, which implies that there is a higher possibility for the formation of a more stable passive layer on the smoother surface.

According to Table 2.4, Cr_2O_3 also showed a significant increase of 10.1% on the surface for sample G1200 compared to 0.5% for sample G240 after corrosion.

Table 2.4 Area percentage of two types of samples.

% Area	G 240	G 1200
Cr_2O_3 (Before)	94.6	88.4
Cr_2O_3 (After)	94.1	98.5
Change in Cr_2O_3	0.5	10.1

Figure 2.7 shows the fitting curves of chromium (Cr 2p) for two types of samples before and after corrosion. Both samples have almost the same binding energies and peak locations for different elements before corrosion. The reason is because surface roughness has not changed the chemical composition of the surface. In order to compare the alternations of the amount of Cr_2O_3 formed before and after corrosion on G 240 and G 1200 sample surfaces, the area under each curve should be calculated. The area of each curve can be obtained by the integration under the curve. From the area% provided in Fig. 2.7, it can be seen that Cr_2O_3 constitutes the majority of the fitting curves shown in the spectra. Even though relatively less Cr_2O_3 appeared

on the surface of G 1200 before corrosion, there was a relatively significant increase of Cr_2O_3 formed on the surface after corrosion.

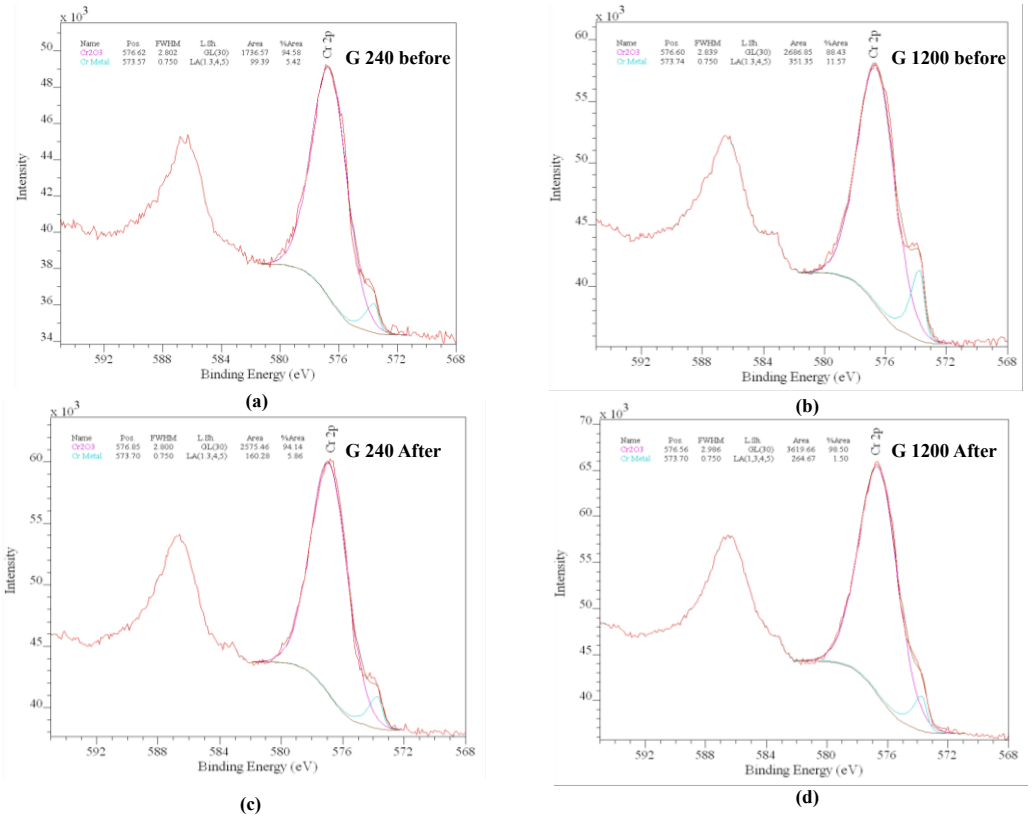

Figure 2.7 High-resolution XPS spectra of Chromium (Cr 2p) of (a) G 240 (b) G 1200 before corrosion, (c) G 240 and (d) G 1200 after corrosion (Color figure online).

2.4.5 AFM

Figure 2.8 illustrates AFM 3D images of samples G240 and G1200 as representatives of a rough and a smooth surface before and after corrosion. As can be seen, as grit number increased, the roughness decreased before corrosion testing. The same trend is almost seen after corrosion testing. All samples, however, show higher roughness after corrosion testing. Figure. 2.8 (a) and (b) show the 3D topography

images for samples G240 before and after corrosion tests. It is obvious that more features, which could be indicative of corrosion products, with a relatively higher height (the highest point on the surface was around 2.5 µm) are formed on G 240 sample surfaces after corrosion, suggesting a more intensive corrosion events. It is said that the diffusion of corrosion products in deeper grooves is limited, and hence, the solution condition for local dissolution of metal is easily satisfied [79]. This means that on rougher surfaces, more metastable pits are formed and the active sites on these surfaces have lower openness (ratio of width to depth at opening of the grooves), hence have a higher possibility to grow larger. But on smooth surfaces, it is more difficult to form micro pits [79]. According to 3D images in Fig.2.8 (c) and (d), there was no significant change in the surface appearance of smoother surfaces after corrosion. This is in agreement with SEM images, *in situ* observations, and corrosion measurements.

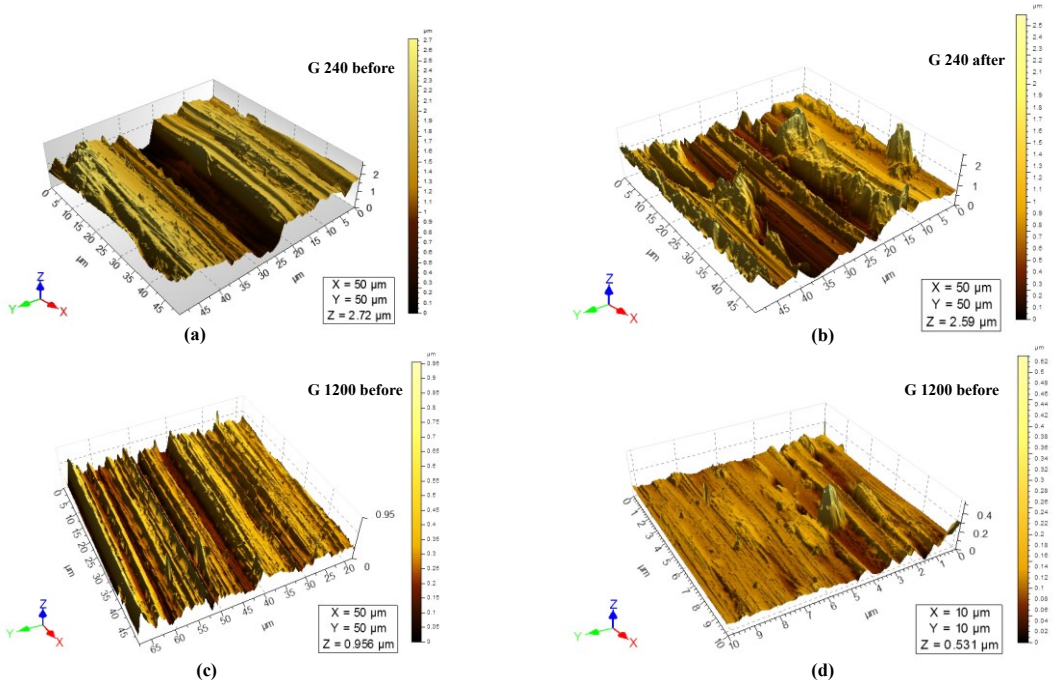

Figure 2.8 AFM 3D images for samples G240 (a) and (b) and G1200 (c) and (d) before and after corrosion.

2.5 DISCUSSION

Based on the measured corrosion potentials and currents, it can be concluded that the corrosion of SS 316 LVM increased with an increase of surface roughness. The reason for this phenomenon is that by increasing the roughness, the number of active sites increased, while deeper grooves played a significant role as suitable sites for localized corrosion [68]. The depth of the valleys that influenced the diffusion of active ions during corrosion and IR drops in the deep valleys also seem to be important parameters that affect the corrosion [80]. On rougher surfaces, compared to smooth surfaces, diffusion processes at nucleation sites in small scratches are hindered and there is a higher probability of accumulation of aggressive species, and the geometry of small scratches makes it easier to maintain a high potential drop [76]. But when the surface is smooth, the pit will survive more due to the formation of lace cover on the pit mouth maintaining the diffusion process, which will result in less corrosion on the surface. It is also said that on the rougher surfaces, the grooves trap the corrosion products, which results in more pitting [80]. In a smooth surface, the frequency of metastable pitting is reduced because the number of available metastable pit sites is reduced and consequently the corrosion is decreased [66]. Also on smooth surfaces, weak points are less ‘‘active’’ than on rough surfaces and the formation of a stable passive film on smooth surfaces is more likely to occur. On smoother surfaces, the total number of active sites, which are available at each potential, is smaller. Additionally, the probability for metastable pits to attain stability on the smoother surface is less than the rougher ones, because the sites are more open.

Rougher surfaces, however, tend to have a larger surface area due to relatively

large amount of grooves and scratches, which will result in more contact area and consequently more corrosion compared to smoother surfaces [66]. Rougher surfaces of a metal also exhibit lower pitting potentials because the roughness causes, less-open pit sites to be maintained during their early stages of growth as metastable pits. Therefore, there is more restricted diffusion of metal cations during propagation, which will result in the transition from metastable to stable pit growth to be made at lower potentials and consequently lower the pitting potential. It is said that a deeper, less-open pit site has a greater probability of generating a pit, than a shallower, more-open one. Since the sites on the rougher surfaces are more occluded than those of smoother surfaces, it follows that pits growing on the rougher surface have a greater chance of survival to the stable growth stage, and thereby show a lower pitting potential [65].

It is also said that, on an active-passive metal, rougher surfaces are more susceptible than smoother surfaces to localized forms of corrosion such as pitting and crevice corrosion. This effect can be related to the surface nucleation of metastable pitting preceding propagation of pitting. Although a higher number of nucleation events take place on a smoother surface as compared to a rough surface, propagation of the pits and formation of micro pits do not occur as readily [67,79]. On a rougher surface, several of these nucleation events will lead to propagation of pits and thereby corrosion. In this research also as discussed in corrosion measurements, SEM, EDS, and AFM results, more corrosion was observed on rougher surfaces.

Figure 2.9 shows the variation of stable pitting potential versus the surface finish of SS 316 LVM samples. As can be seen, by decreasing the surface roughness, the average value of time of stable pitting has increased confirming a postponed pitting

for the smoother surfaces. Figure 2.10 also illustrates the change in pitting potential for different surface roughness of SS 316 LVM. Smoother surfaces show a more noble average potential identified with error bars.

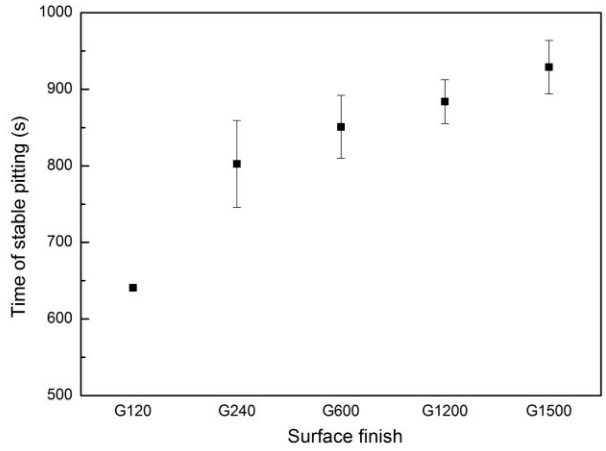

Figure 2.9 Variation of time of stable pitting potential vs. the surface finish.

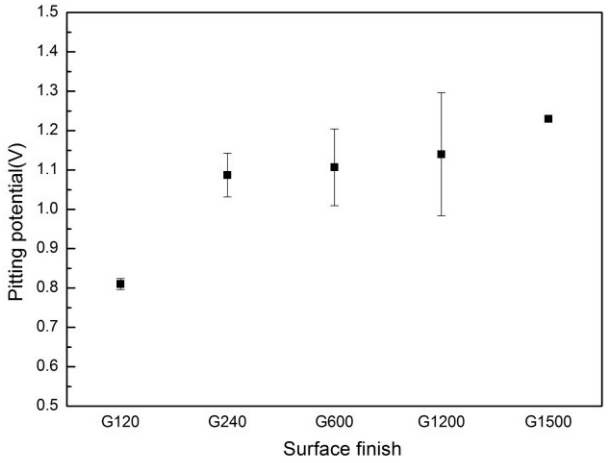

Figure 2.10 Variation of pitting potential vs. the surface finish.

EDS results for oxygen and chlorine content on the surface after corrosion also confirm the corrosion results. All the EDS results of SS 316 LVM samples in this study showed an increase in oxygen content after corrosion. For surfaces with low roughness values, this increase in oxygen content can be more related to the oxide layer formation, and for rougher surfaces, it can be related to both the formation of a passive layer and more corrosion products [68]. Such a passive film for smoother surfaces would provide better corrosion protection, as evidenced by these samples showing the lowest corrosion for the samples. Higher chlorine content on rougher surfaces also confirms more corrosion products and corrosive ions trapped on the surface. *In situ* observation of corrosion, SEM, and AFM also confirmed more corrosion on rougher surfaces of SS.

XPS also confirmed that although there was more oxygen on a rough surface before corrosion, more oxygen, chromium, and iron were found on the surface of sample with lower roughness after corrosion. The result of a higher amount of oxygen detected on a rough surface before corrosion can be attributed to the combined fact that more exposure of the rougher surface in the air led to a higher content of the naturally formed passive layer. However, higher amount of oxygen after corrosion can be related to the formation of chromium and iron oxides in the passive layer resulting in higher corrosion resistance of smoother surfaces. The significant increase in the area covered by Cr_2O_3 on smooth surface compared to rough surface also confirmed corrosion results.

2.6 CONCLUSIONS

This study showed that surface morphology has a significant effect on corrosion

of SS 316 LVM in 0.9% (by mass) NaCl solution. According to potentiodynamic polarization measurements, as surface roughness decreased, the pitting potential shifted to more noble values. On rough surfaces, there is a greater contact area between the corrosive medium and metal together and there are more active and weak sites, and there is limited diffusion out of the deep grooves; grooves trap the corrosion products; but there is fast formation of a stable oxide film on the smoother surfaces that improves its corrosion performance. In the case of active-passive metals including, nickel, aluminum, and stainless steel, the rougher surface would be easily pitted because the smooth surface has fewer sites for pit nucleation and can quickly form a passive film to prevent pit nucleation. AFM showed an increase in roughness because of formation of more corrosion products of rougher surfaces. *In situ* microscopic observations and SEM confirmed the conclusion of more corrosion on rougher surfaces. EDS and XPS also showed the change in different elements including oxygen and chromium on the surface after corrosion.

CHAPTER 3 THE EFFECT OF SURFACE PATTERNING ON CORROSION

The effect of Surface Patterning on Corrosion Resistance of Biomedical Devices- A Heterogeneous Wetting Approach

Authors: Mengnan Guo, Alisina Toloei and Harm H. Rotermund

Department of Physics and Atmospheric Science, Dalhousie University, 6310 Coburg Road, Halifax, Nova Scotia, B3H 3J5, Canada.

All figures, texts were contributed by Mengnan Guo. Alisina Toloei and Harm H. Rotermund contributed editing and modification.

Submitted to Journal of Materials Engineering and Performance, September, 2015.

3.1 ABSTRACT

In this study, two styles of surface topographies have been created on stainless steel wires to test their corrosion resistance as simulated implanted biomedical devices. Grade 316 LVM stainless steel wire was initially polished to G1500 surface finish before treatment to produce the two different topographies: 1.) Unidirectional roughness was created using SiC papers and 2.) Various patterns were created with specific hole diameter and inter-hole spacing using Focused Ion Beam (FIB). In order

to simulate the environment of implanted biomedical devices, a three-electrode electrochemical cell with 0.9% (by mass) NaCl solution has been used to test the corrosion resistance of the samples by potentiodynamic polarization test method. SEM and EDS analyzed the appearance and chemical composition of different elements including oxygen on the surface. The potential of stable pitting, time related to the initiation of the stable pitting, and the highest corrosion current associated with stable pitting have been compared for samples with the two styles of topography . It was found that surfaces with patterns have a relatively high pitting potential and it takes longer time to initiate stable pitting than the surface without any patterns.

3.2 INTRODUCTION

Metallic biomaterials have a relatively long history among the various biomaterials [81]. Among the main metallic materials for biomedical applications, titanium and its alloys, Co-Cr-based alloys, stainless steel 316LVM, and magnesium alloys are the most vital materials for biomedical and dental applications because of their comparatively high corrosion resistance and good bio-compatibility in the human body [82–87]. However, due to the cost and scarcity of noble metal and its alloys, stainless steel receives much attention for its high mechanical strength and relatively high resistance in many corrosive environments, due to the presence of a nano-scale chromium oxide film or the protective oxide layer that spontaneously forms on its surface and acts as a barrier against aggressive diffusive molecules in the surrounding environment [29,88]. Stainless steel was first used successfully as an implant material in the surgical field after aseptic surgery was established [82]. However, stainless steels suffer from insufficient corrosion resistance against pitting corrosion in strongly

aggressive media containing S^{2-}, Cl^- or other halide anions. A natural passive film forms *in situ* on the surface but does not provide an effective enough corrosion protection [83,89], thus further improvements in corrosion resistance are required for its safe use as an implant material.

Different types of corrosion prevention methods have been considered for improving the corrosion resistance and performance of stainless steel in biomedical applications. The majority of works have focused on the application of corrosion resistant coatings or protective films on the surface of stainless steel, including atomic layer deposition, arc ion plating, ion-beam-assisted sputtering, and tungsten inert gas deposition [83,88,90–92]. Other researchers suggested that organic-inorganic hybrid coatings produced by sol-gel methods have significant impact on the enhancement of corrosion resistance by increasing the pitting potential and decreasing the current intensities of stainless steel intended for biomedical applications [93–96].

Other corrosion prevention methods such as alloying of the steel and the modification of surface oxide layers have been also performed to improve corrosion performance [6,60,63]. Mohd Talha et al. improved the compatibility and corrosion properties by the replacement of nickel with nitrogen for austenitic stainless steel, which results in better corrosion and wear resistance, and superior biocompatibility [97]. Chun-Che Shih et al. studied the properties of surface oxide on corrosion resistance of 316L stainless steel for biomedical applications, which showed that stainless steel wire passivated with an amorphous oxide film exhibits the best corrosion performance *in vitro* corrosion resistance and it is found to be the best surface protective film for cardiovascular devices [37]. A. Shahryari et al. enhanced the

corrosion resistance of grade 316 LVM stainless steel by electrochemically forming highly protective passive oxide films on the material's surface, which showed that the film formed in the nitrate electrolyte to be completely resistant to pitting in physiological simulating electrolytes (PBS and Hank's) and it offers very high pitting corrosion resistance in the pure saline electrolyte [98,99].

Another method for improving corrosion properties is surface modification without using chemicals or surfactants [54,68,69,100]. Surface modification has the distinct advantage that it avoids complications associated with releasing toxic ions into human tissues from certain organic coatings or chemical elements embedded in the material [101,102]. For active-passive metals the researchers showed that by decreasing the created unidirectional roughness (increasing the SiC paper grit number from G60 to G1200), corrosion resistance improved [68]. A patterned surface with heterogeneous solid-liquid interface is also notable for its liquid repellency and low surface energy, which will have vast potential in various applications [54,103]. A.S. Toloei et al. first showed the effects of various types of surface patterns and its relationship with corrosion resistance of active-passive metals, which indicated better corrosion resistance, compared to the polished reference samples [54]. In this work, the main focus is to enhance the corrosion resistance of grade 316 LVM stainless steel by the creation of various types of surface topographies. A comparison is also made between the smoothest surface (most corrosion resistant surface [68]) and the designed patterned surface. The effects of different surface pattering on pitting potential, time of the initiation of stable pitting, and average peak values of current were also compared among samples with and without surface patterns.

3.3 EXPERIMENTAL PROCEDURES

3.3.1 Materials Preparation

The wire samples used were low carbon stainless steel (SS 316 LVM) with a 0.381mm (0.015 in.) diameter (Smallparts Inc.) Twenty wires in total were held by the sample holder mounted with Crystalbond adhesive. All samples were initially prepared to a highly smooth surface of G1500. Subsequently, one set of samples was given a unidirectional roughness using SiC papers and the second set was prepared with surface patterns created with FIB. Before creating patterns on the surface of the samples, all the samples have been ground by incrementally finer SiC papers (G120, G240, G600, G1200, and G1500) until reaching the final surface finish of G1500. The direction of the sample holders would be turned by 90 degree against its original direction when moving to a finer SiC paper in order to remove the grooves produced from the previous step. All of the samples have been cleaned by high purity deionized water (18 $M\Omega\ cm^{-1}$ Nanopure) before the start of the experiments. The electrolyte was a 0.9% NaCl solution (by mass) which was used to mimic the environment of implanted biomedical devices, and was filtered through a 0.2 μm filter before being put into the electrochemical cell. The wires were then bent into L shape so that they could be inserted into the access ports on the top of the cuvette (solution container). Samples were finally coated three times with a clear lacquer. Wire faces were inspected with an optical microscope and additional cleaning was done if it was necessary. All the wires were kept for 30 minutes until the lacquer completely dried, and then inserted in to the cuvette containing the NaCl solution. All samples have been immersed into the solution for the duration of 30 minutes before conducting the experiment to reach a stable

potential.

3.3.2 Instruments

Focused ion beam (FIB) method was used utilizing a Hitachi FB-2000A machine to create the patterns on the surface. The holes had a diameter of 30 micrometers with center-to-center spacing of 60 μm a depth of 20-25 μm. In our research, liquid metal ion source (LMIS) of gallium was selected to bombard the substrate for micro-fabrication process. The total time for creating the patterned surface required 6 hours, and the same ion beam was used to provide images as well.

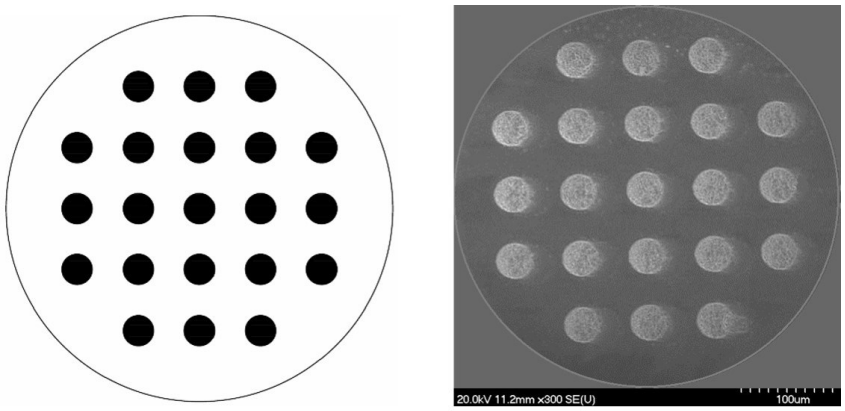

(a) (b)

Figure 3.1 Images of surface patterns for G1500 stainless steel 316 LVM surface, (a) a simple sketch of patterns designed by Autocad, (b) SEM images of real surface patterns.

Figure 3.1 shows the simple sketch of the patterns created on the surface of wire sample and scanning electron microscope (SEM) image of actual holes in the surface. For the electrochemical corrosion tests, a three-electrode configuration was used: an Ag/AgCl wire was chosen as the reference electrode, a platinum wire served as the counter electrode, and a prepared stainless steel wire was used as the working electrode.

The potentiostat used was a Fritz-Haber-Institute, Berlin-ELAB-G050-29 mode. The initial potential was scanned from -600 mV until it reached 0 mV. It was then raised in 100 mV steps at ramp rates of 10 mV/s, holding at each step for 1 min. After a sudden increase of current, the potential was then reversed to its initial value of -600 mV. Another type of test which associated with non-stop potential measurement, has been performed with the same scan rate at the initial potential of -600 mV, and the potential has been reversed to its starting value once there is a steady increase in the current. The purpose for doing this type of test is to compare the behavior of the same type of samples with two different methods of anodic polarization tests with different timings. In order to observe the stable pitting, the potential was continuously increased if no pitting events could be observed at up to 800 mV (the highest potential value), and the positive scanning would be terminated and reversed at the stage of stable pitting. To verify the pitting events that occurred on the polished surface, i*n situ* optical techniques were employed. In order to visualize the pitting process, background subtracted contrast enhanced microscopy was used during corrosion testing. SEM was used to obtain the actual appearance of sample surface by a HITACHI S-4700 model microscope. The accelerating voltage, emission current and working distance used were 20 kV, 15.5 μA and 11.2 mm respectively. Energy dispersive X-ray spectroscopy (EDS) was also carried out with the same machine to analyze the chemical elements on the surface. Figure 3.2 illustrates the alignment of the optical set up used in the lab to observe the changes on the surface during corrosion testing. The uncoated surface of stainless steel wire was imaged by the perpendicular incident light from the optical microscope, which recorded the in-situ images onto the chip of a charge-coupled device

(CCD) video camera. Any stable pitting events associated with a sudden dramatic change in terms of spikes were either shown as dark spots or the blurring edges of the unit holes created on the surface. Another part of the set-up is related with ellipsometry for surface imaging (EMSI), which could be used as complementary techniques to visualize the changes of the thickness of the surface oxide layers on mirror- like surface before and after corrosion. Monochromatic laser light is elliptically polarized by means of a Glan–Thompson prism polarizer and a quarter wave plate compensator, in such a way that after reflection at the sample the light is linearly polarized and therefore can be annihilated by a second Glan–Thompson prism analyzer [78]. However, in our work, since the samples G 1500 were not able to reach the level of mirror-like smoothness, EMSI was not useful for illustrating of surface changes associated with corrosion tests. But the surface change was observed and filmed.

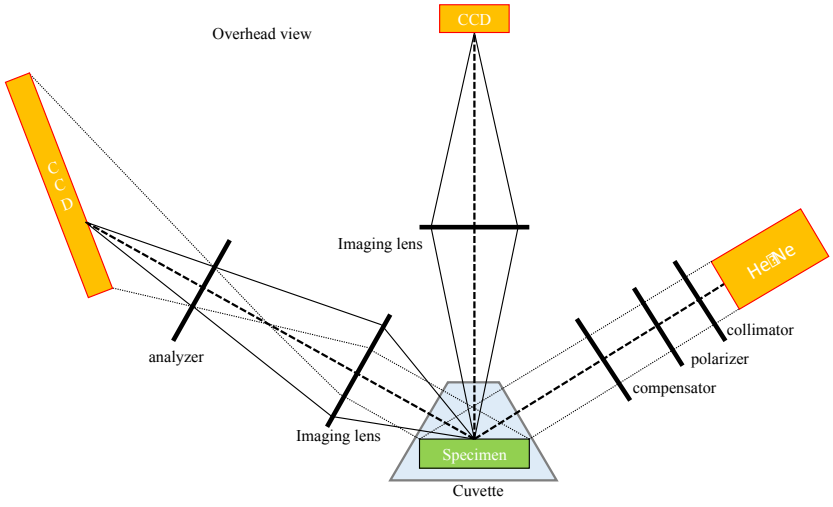

Figure 3.2 A simple sketch of optical set up.

3.4 RESULTS AND DISCUSSION

3.4.1 Corrosion Testing

Figures 3.3 (a-c) show typical current and potential values versus time for sample G1500 and the patterned sample. Figure 3(a) displays the current versus time plots in stop tests, where potential has been held in steps of 100 mV for one minute after 0 mV. Figure.3.3 (b) shows the current versus time plot while there was no stop in potential measurements (continuous scan), and Figure.3.3 (c) illustrates the potential versus time plot of the stop tests with holding potential in steps of 100 mV. By creating patterns on the surface of stainless steel wires, the average time until initiation of stable pitting has been increased from 890 s to 1053 s for five samples, which indicates a higher level of corrosion resistance on the patterned surface. An examination of the highest stable pitting current revealed the fact that the sample with surface patterns generated a lower degree of pitting current than that of the surface with fine unidirectional roughness.

Figure 3.3 (b) shows the current versus time plot for anodic polarization tests with no stops for the potential. The trend related with the initiation time of stable pitting and the highest pitting current for these two samples is consistent with the results obtained from the stop tests in Figure 3.3 (a), which indicated that sample G 1500 with patterned surface has a relatively higher corrosion resistance due to the delay of launching stable pitting and the lower value for pitting current. Figure 3.3 (c) illustrates the potential versus time plot of the stop tests with holding potential in steps of 100 mV for both samples. In both plots, the potential has been reversed once the stable pitting phenomenon happened on the surface of the samples. Comparison of patterned and

G1500 samples suggested the enhanced corrosion resistance of the sample G 1500 with surface patterns, which can be attributed to the increase of the final stable pitting potential. The average values of the breakdown potential (i.e. the potential associated with initiation of stable pitting) have been increased from 1.25 V to 1.48 V. It can be seen as an obvious potential jump in Figure 3.3 (c). A possible explanation for this phenomenon is that the contact area between the stainless steel surface and the electrolyte solution has decreased due to the existence of a heterogeneous interface, which leads to indirect contact of the corrosive electrolyte [54]. This can be attributed to the heterogeneous wetting- alternating solid-liquid zone and stable air/vapor pocket inside the holes [51,54,104].

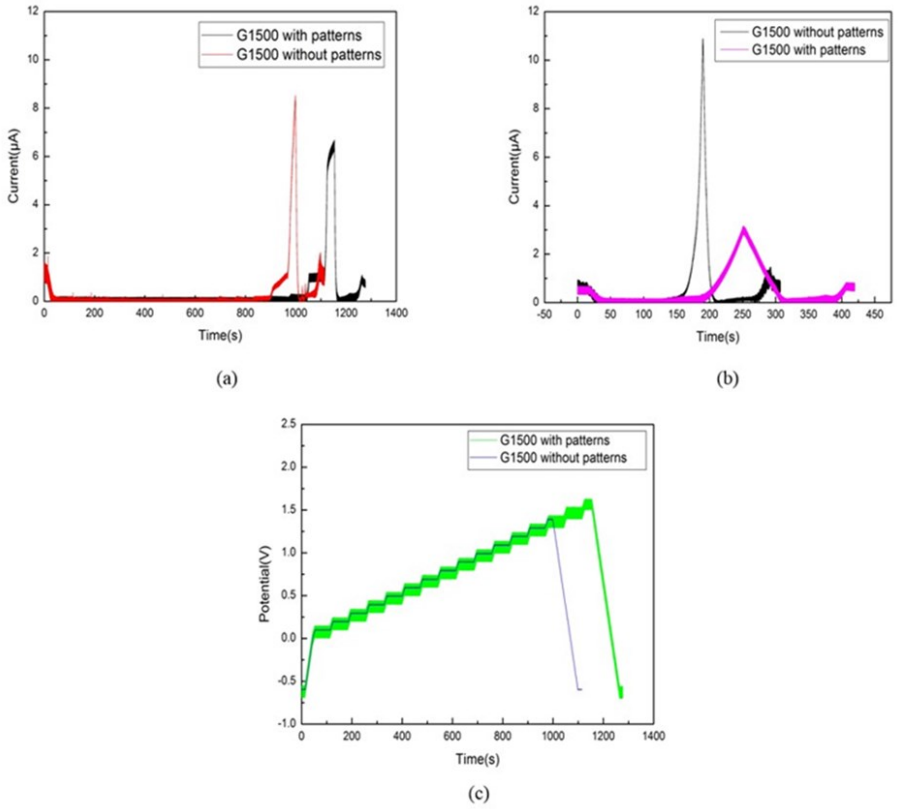

Figure 3.3 (a) The Overlay of current versus time for stop test, (b) current versus time for non-stop test and (c) potential versus time for samples G 1500 and patterned sample.

Table 3.1 Gives the pitting potential, critical current of pitting and the initiation time associated with pitting of sample G1500 with and without surface patterns. In each case the measurements were carried out for five samples. By comparing all the results, it is apparent that the samples with surface patterns exhibit a relatively higher corrosion resistance compared to samples without the patterns, because of a high stable pitting potential, lower values of critical pitting current and the postponing of the time related with the onset of stable pitting.

Table 3.1 E_{pit}, $I_{critical}$ and time values of initiation of pitting for sample G 1500 with and without surface patterns.

Sample (G1500)	$E_{pit(stop)}$/V	$I_{critical(non-stop)}$/ μ A	$I_{critical(stop)}$/ μ A	Time of stable pitting/s
without patterns	1.25	8.34	8.47	890
with patterns	1.48	3.18	6.67	1053

3.4.2 SEM

Figure 3.4 (a) and (b) shows the SEM micrographs of the patterned sample before corrosion testing. A careful observation of SEM micrographs in Figure 4. (c and d) shows no significant change in the appearance of the patterned sample after the samples underwent the electrochemical corrosion test, which clearly indicate that no significant corrosion happened on the surface of the patterned sample which confirm the corrosion testing results. Figure.3.4 (b) and (d) illustrate the SEM images of a unit hole, in which (b) stands for topography of the unit hole before corrosion and (d) represents the hole after corrosion. Severe localized corrosion, specifically pitting corrosion, was not observed throughout the surface, indicating the fact that the patterns formed on the surface act as an effective method to decrease pitting corrosion.

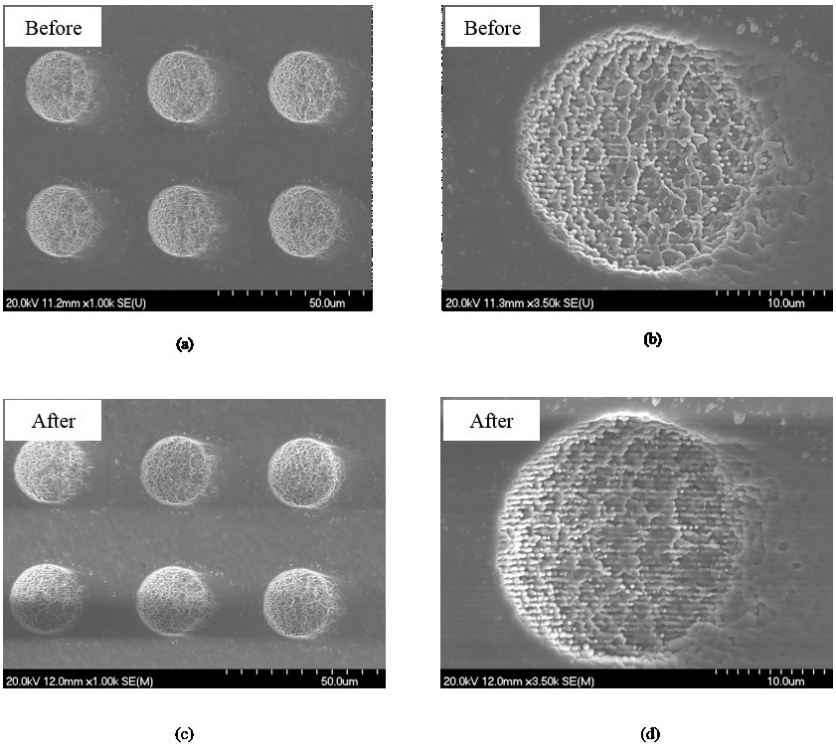

Figure 3.4 SEM images of unit holes created on the sample surface before and after corrosion.

3.4.3 EDS Analysis

EDS results shown in Figure 3.5 and Table 3.2, give the details of the regions where the oxygen content inside and outside the hole have been measured. Even though the oxygen content from the EDS data shown in Table 3.2 has a great increase outside the hole, it exhibits an even more significant increase in the weight percentage of oxygen inside the holes after corrosion. So, there are more oxygen and chromium inside the holes (i.e a more stable passive layer). After corrosion the oxygen content was 1.35 wt% and 2.46 wt% outside and inside the holes respectively. Chromium average weight percent inside the holes was 20.33%, whereas there was just 15.95% of chromium outside the holes. This is an obvious indication that oxide layers including

chromium oxide have been formed both inside and outside of the holes; however, the oxide layers located on the surface, that is outside of the holes were dissolved more by the electrolyte. A plausible explanation of this phenomenon could be attributed to the decrease in the possibility for electrolyte to contact the bottom of the holes, which was less likely to destroy the passive layer formed as the protective layer inside the holes. Thus, the thickness and the total amount of the passive layer formed on either the surface inside or outside of the holes are associated with the contact with the electrolyte. As it is known, the less the contact area between the surface and the corrosive electrolyte, the lower will be the corrosion. This can be attributed to the heterogeneous wetting that existed between the surface and the solution, which created alternating solid-liquid zones and a stable air/ vapor pocket [105,106]. Heterogeneous wetting, noted as the Cassie-Baxter state [51,104,107], can be used to create an effective air/vapor region trapped in the topographies of the surface, where aggressive ions have less possibility to contact the inner surface directly.

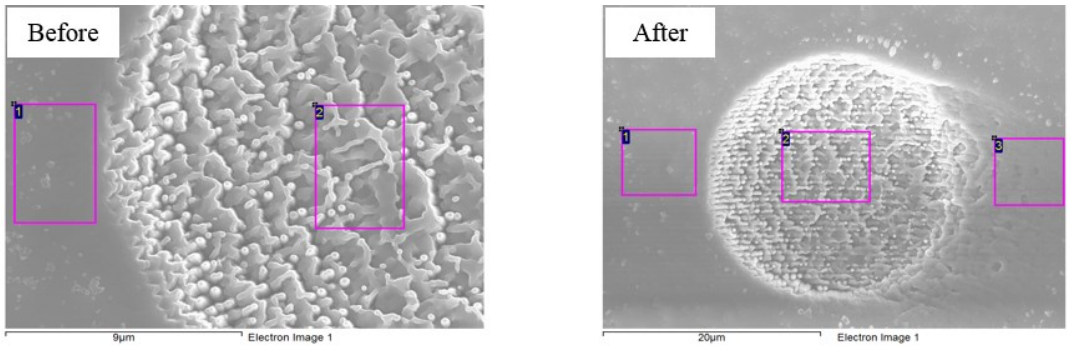

Figure 3.5 EDS images inside and outside of the holes created on the sample surface before and after corrosion.

Table 3.2 Average oxygen content before and after corrosion tests

O wt%	Before test	After tests	Change in Percentage
Surface	1.12	1.35	17%
Hole bottom	1.18	2.46	52%

3.5 DISCUSSION

Even though the theory of heterogeneous wetting has not been explicitly discussed in this study, the existence and the vital role of heterogeneous interface can be applied for the observed increase in corrosion resistance in the patterned samples. This can be concluded based on the results of three independent types of experimental studies: SEM, EDS and potentiodynamic polarization tests. The arguments in support of the existence of the heterogeneous wetting can be summarized as follows. Comparison between the data from current and potential versus time of sample G1500 from potetiodymanic polarization tests showed the delay of the initiation of the pitting, increase in the stable pitting potential and the decrease in the critical current value for the patterned samples, suggesting that samples with surface patterns exhibits higher corrosion resistance in the simulated biomedical NaCl solution.

Figure 3.6 shows the pitting potential and initiation time of stable pitting versus surface finish. It is apparent that sample G 1500 with surface patterns exhibits an obvious increase in corrosion resistance, which is corresponding to the increased pitting potential [108]. Also, the retardation of the initiation of pitting can also be observed in Figure 3.6 for the patterned sample. Both plots are confirming the fact that surface patterns created on sample G 1500 acts as an effective way to improve the corrosion

resistance of stainless steel 316 LVM in the simulated biomedical solutions (0.9% by mass NaCl).

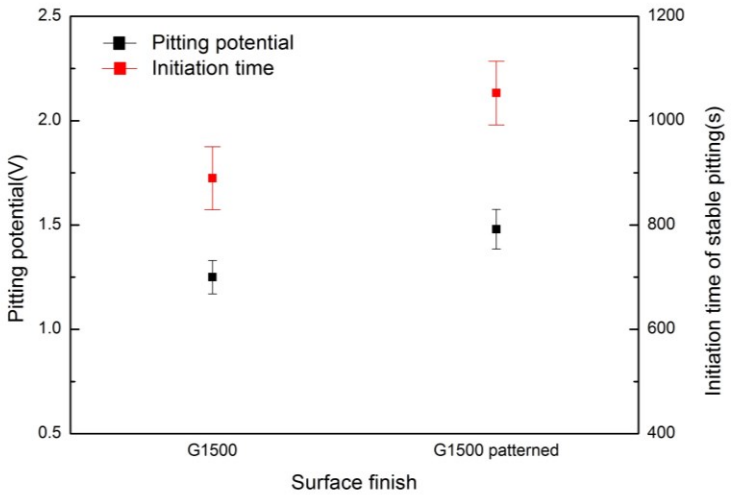

Figure 3.6 Variation of pitting potential and initiation time of pitting with different surface finishes.

The theory can also be confirmed further by the microstructural analysis (SEM), which showed that there was no significant detectable change in the microstructure of the patterned samples after corrosion tests. Chemical composition data from the EDS analysis shown in Table 3.2 also illustrated an obvious increase in the weight percentage of oxygen content inside the hole (52%) after corrosion, which is more than 17% on the surface for the sample G1500 with surface patterns. A higher weight percent of chromium was also found inside the holes indicating more oxide layer inside the holes. These results led to the conclusion that a possible explanation of the observed improvement of corrosion resistance is due to the decrease of the overall electrolyte/metal surface contact area, indicating that the passive layers have been formed and the rapid convective motion and contact between the electrolyte and the

surface could lead to the dissolution of the passive layer formed on the surface outside the holes [54]. It is clear that the electrolyte/metal surface interaction is different inside the holes of samples with decreased corrosion, and the heterogeneous wetting can be proved since the passive (oxide) layer formed on the surface during the corrosion tests were susceptible to dissolution by the electrolytic fluid, while the layers located inside the holes were unlikely to be removed due to the protection by air/vapor pockets created by the alternating liquid and vapor zones [105,106].

3.6 CONCLUSIONS

Arrays of surface patterns have been created by focused ion beam on stainless steel 316 LVM samples. The surface patterns played a vital role in the enhancement of corrosion resistance for stainless steel in the biomedical simulated solutions. It has been shown that a possible reason for the increase in corrosion resistance is the heterogeneous wetting which formed on the patterned surface as evidenced by the corrosion testing, SEM and EDS analysis of the patterned surfaces.

CHAPTER 4 THE EFFECT OF WATER TREATMENT ON CORROSION

The Enhancement of Corrosion Resistance of Stainless Steel 316 LVM in Biomedical Devices by simultaneous Effect of Surface Morphology and nanopure Water

Authors: Mengnan Guo, Alisina Toloei and Harm H. Rotermund

Department of Physics and Atmospheric Science, Dalhousie University, 6310 Coburg Road, Halifax, Nova Scotia, B3H 3J5, Canada.

All figures, texts were contributed by Mengnan Guo. Alisina Toloei and Harm H. Rotermund contributed editing and modification.

4.1 ABSTRACT

Stainless steel 316LVM is an alloy, which has been widely used in medical and biological implantations due to its excellent corrosion resistance to general corrosion. Nevertheless, steels often suffer from localized forms of corrosion such as pitting corrosion. In this study, in order to improve the corrosion resistance of stainless steel 316 LVM, the simulated biomedical environment with NaCl (0.9 %) by mass was used. In total, two types of samples were created. 1). Samples were polished with different grits of SiC papers to reach unidirectional roughness. 2). Samples with different

unidirectional roughness surface finishes also went through 90 °C nano pure water treatment for the durations of three hours. *In situ* observation with optical microscope was performed to visualize the alternations on sample surfaces during corrosion tests. Scanning electron microscopy (SEM) and energy dispersive X-ray spectroscopy (EDS) were conducted to perform surface analysis on sample surfaces after corrosion.

4.2 INTRODUCTION

Stainless steels are generally considered to be corrosion resistant to uniform corrosion. This phenomenon originates from the fact that nickel and chromium spontaneously form thin passive oxide layers on the surfaces, which plays the role as protective barriers against any further direct contact from its corrosive surroundings [109]. However, under certain specific conditions, stainless steels are prone to localized corrosion, for instance pitting corrosion. The most commonly aggressive ion is the chloride anion found in many natural and industrial environments as well as human bodies [58]. Pitting is generally initiated at sites of local heterogeneities, such as scratches, defects, inclusions and grain boundaries [29]. The idea that manganese sulfide (MnS) acts as a vital role as the initiation center of pitting on stainless steel can be traced back to nearly 40 years [20,110] and has continuously been considered as a possible reason into recent years [20,21,23]. For instance, Klages et al used high temperature nano-pure water bath to improve the corrosion resistance of the stainless steel 316 LVM by reducing the number of MnS inclusions from the surface [29]. In our study, in order to further improve the corrosion resistance of stainless steels, a combined method which takes into account of the effect of surface roughness and nanopure water treatment has been investigated.

The mechanism of pitting has been divided into three stages, initiation, metastable propagation and stable propagation of pits [6].The first step is initiated by a local breakdown of the protective oxide layer as a result of the invasion from aggressive anions on the surface. Generally, the corrosion rate is increased by the fact that even more aggressive environment is produced by the corrosion reaction itself. This often happens soon after the earlier stages of pit propagation, when the pits are still quite small (pit at this stage is often of a few micrometers), re-passivation process occurs spontaneously and inhibit any further progress on pitting corrosion. The third stage of stable propagation is reached when spontaneous re-passivation is no longer exit [7,20,111,112].

Several possible ways of the improvement of the resistance of stainless steel have been proposed from previous research works, such as alloying, application of organic coatings, and surface modifications [6,7,35,60,62,64,93,95,113]. Among the various corrosion prevention methods, mechanical surface modifications on the material itself turned out to be a promising way for the enhancement of the corrosion resistance. In our study, the enhancement of corrosion resistance related with metastable pitting of stainless steel 316LVM has been investigated.

Based on the theory and research work presented in the literatures, the experiment conducted in this paper were related to the modification of the sample surfaces not only by applying simple mechanical grinding to produce different surface morphologies, but also adding nanopure water treatment at elevated temperature on the surfaces of newly polished stainless steel 316 LVM samples.

4.3 EXPERIMENTAL PROCEDURES

4.3.1 Material Preparation

Stainless steel 316 LVM with 0.381 mm in diameter from Smallparts Inc was used in this study. Surfaces of the samples were the critical places where electrochemical tests were performed. Sample wires were mounted by the adhesive Crystalbond in the sample holders and polished with SiC papers of grit 120, 240, 600, 1200, and 1500. For instance, to produce the surface to G 1500, samples were polished in steps of SiC papers staring from the roughest one (G 120) to the smoothness one (G 1500). Also, samples were rotated by 90 °C for each grit of SiC papers used, so as to produce unidirectional roughness at the end. Eventually, 5 level of surface smoothness were created on sample surfaces. All of the surfaces of sample wires were cleaned by deionized water (18 MΩ cm-1) after mechanical grinding. Figure 4.1 illustrates one of the finished sample with the end of the wire with a mirror like surface [29]. One set of the samples first underwent the mechanical grinding by using five types of SiC papers, and then they were treated with nanopure water at elevated temperature (90 °C) for the durations of 3 hours. The other set of samples went through the same levels of mechanical polishing. Both types of samples were painted with a red nail polish coating under a stereomicroscope along the wire except for the cross-sectional area at the end of it, and that only this polished faces of wires remained uncoated.

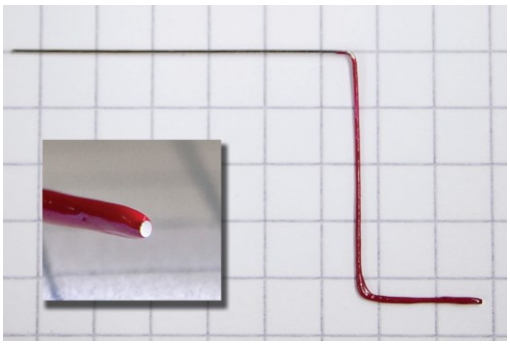

Figure 4.1 A photo shows one of the prepared stainless steel sample wires [29].

4.3.2 Electrochemical Test

A three-electrode system was used to conduct the corrosion tests. The stainless steel 316 LVM sample is the working electrode, Pt. wire serves as counter electrode and Ag/AgCl acts as reference electrode. In order to simulate the biomedical environment inside human body, sodium chloride electrolyte (NaCl) with mass percentage of 0.9 % was used as corrosive solution. The cell of the three-electrode system was a specialized-designed cuvette with dimensions as shown in Figure 1.10 from chapter 1. The solution of NaCl was inserted into the cuvette through a 0.2 μm filter to eliminate impurities from the solution.

Two different experiments of anodic polarizations were conducted with a potentiastat (Berlin-ELAB- G050-29 model) in this work, which were stop tests and non-stop tests. The stop tests were initially scanned from -600 mV with the scan rate of 10 mV/s. Potentials would be increased in steps of 100 mV and halted for 1 minute at each step after passing 0V. Once a dramatic increase in current was observed, this was considered to be the onset of pitting, the scanning direction was then reversed with a scanning rate of 20 mV/s until it went back to -600 mV. Non-stop tests were

performed from the same starting potential at -600 mV with a scanning rate at 10 mV/s, while continuously scanning without holding potentials. Again, the potential was reversed where a significant increase of anodic current happened and stopped at -600 mV.

4.3.3 *In-situ* Optical Techniques

In situ observations were done during the corrosion tests on the sample surfaces with two optical set-ups to detect changes with the formation of pits on the surfaces. The first one is optical microscope. The LED laser lights illuminate the tip of stainless steel sample, which is separated from the imaging path with its charged couple device (CCD) camera (Kappa CF-8). These two optical illumination and imaging are connected though a beam splitter. The lens at the front is not only to focus the laser light on sample surfaces but also to produce a high-resolution image. The optical microscope recorded the video with 25 frames per second with a lateral resolution of approximately 2 μm [3]. Another optical set up was ellipsomicroscopy for surface imaging (EMSI). A collimated HeNe laser beam was sent out by the light sources and went through a linear polarizer and quarter wave plate, which yielded the elliptical polarized light on the right side of Figure 4.3 Laser beam reached sample surfaces that fulfilled the criteria of the Brewster Angle (in our case, it is around 65 °). After reflection, it would be linearly polarized again and could pass through another polarizer located on the left side of the set up [78]. The change associated with the thickness of the oxide layer due to the effect of corrosion can be reflected as the change in the polarization of the light. Due to the sensitivity of EMSI, which normally reaches nanometer scales, only samples with mirror like surface finishes can be well-suited for

imaging by EMSI [31]. Therefore, in our work, it was unfortunate that no useful data of EMSI can be presented for the observation of alternations on the sample surfaces. A simple sketch of two *in situ* optical set-ups and the photo of the optical set-ups in the lab are presented in chapter 3 (i.e. Figure 3.2) and chapter (i.e Figure 2.1), respectively [29].

4.3.4 Surface Analysis (SEM and EDS)

Surface characterization was performed on sample surfaces before and after water treatment to show the different behavior in corrosion performance of samples. A Hitachi S-4700 cold field emission scanning electron microscope (SEM) device was employed to collect the images from sample wire surfaces. Images were taken with at the magnification of 250X, 600X, 1000X and 1500X and at the operating voltage of 20 kV. Energy dispersive X-ray spectrometer (EDS) with the same instrument was used to acquire the information of the chemical compositions on sample surfaces before and after water treatment. The penetration depth of the X-ray beams is around a few microns, which might suggest that the chemical data obtained could possibly contain information beneath the surface layers. Klages et al. used the same technique to show the sulfur content before and after water treatment [29]. The innovation of this work was based on what has been presented from the previous research that water treatment could improve the corrosion resistance of stainless steel, and by treating samples with different surface roughness with nanopure water at elevated temperature, the influences exerted from the combined two methods on the corrosion resistance of stainless steels will be investigated.

4.3.5 Water Treatment

The stainless steel samples were treated in a teflon container for 3 hours at 90 °C in nano pure water. The water inside the container was replaced by pre-heated and fresh water every one hour during the treatment in order to prevent the saturation of dissolution of ions in the nanopure water. Samples were stored in a clean container under argon atmosphere immediately after the water treatment so as to prevent sample surfaces from re-oxidation.

4.4 RESULTS

4.4.1 Anodic Polarization

Figure 4.2 shows plots of potential and current as a function of time in stop tests. There is an increase in both the average initiation time of pitting and pitting potentials from sample G 120 to sample G 1500, indicating the fact that decreasing surface roughness could improve the corrosion resistance of stainless steel.

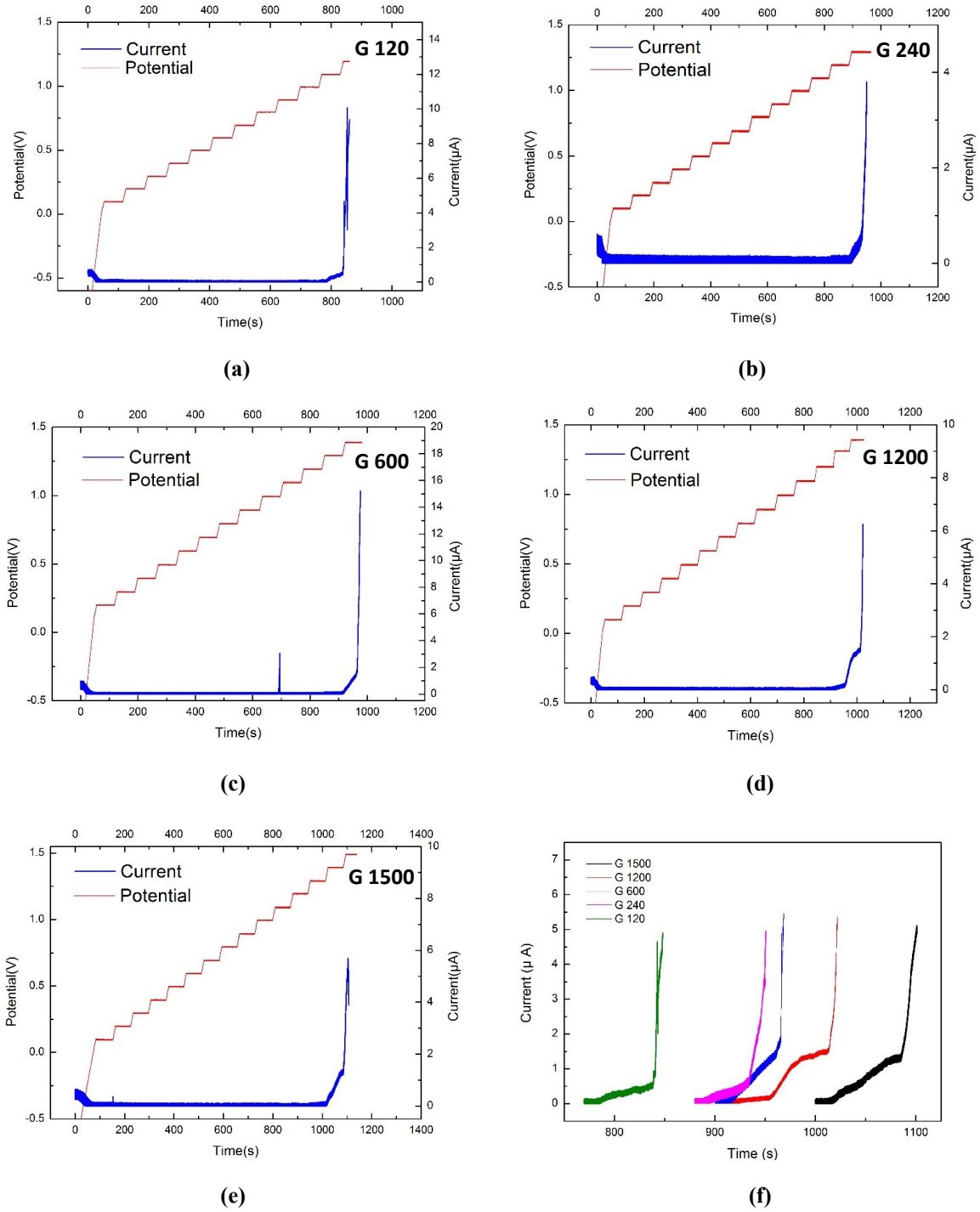

Figure 4.2 Plots of potential and current as a function of time for samples with different surface roughness. (a)-(e): Plots related to potential and current versus time, (f): Plot of current as a function of time treated with nanopure water.

The average pitting potential, increases from 1.09 V to 1.39 V for sample G 120 to sample G 1500. The corrosion parameters associated with pitting potential and the initiation time of pitting related to water-treated samples have been presented in Table 4.2. It can be seen that samples with a smoother surface tolerate the current up to a higher potential. Generally speaking, both the average pitting potential and pitting initiation time have a consistent increasing trend by decreasing surface roughness. Alisina Toloei et al. presented the same results in the research of stainless steel 316 LVM without water treatment in chapter 2 [108].

The last plot of Figure 4.2 shows the sharp changes of current after the onset of pitting events. As can be seen from (f), the selected current range is from 0.1 A-5 A. After the initiation of pitting, it took a longer time for relatively smooth surfaces to exhibit a sharp increase in current. For instance, a plateau appeared after the initiation of pitting for G 1200 sample, which suggested the fact that the current change was retarded between 950 to 1000 s. Apparently, the onset time of a huge increase in current is postponed due to the simulated effect of surface roughness and nanopure water treatment. All the samples follow the same trend, which suggested that corrosion resistance of stainless steel 316 LVM could be further enhanced by treating smoother samples with nanopure water treatment at elevated temperatures.

Table 4.1 presents the times at which the current changed from 0.1 A to 5 A. T_1 and T_2 stand for the time when the current is at 0.1 A and 5 A, respectively. This phenomenon indicates an enhanced performance in terms of corrosion resistance of samples with the assistance of the combined effect of reducing surface roughness and nanopure water treatment.

Table 4.1 Parameters associated with time of selected regions.

Grit	T_1/s	T_2/s
120	793	848
240	902	978
600	918	970
1200	931	1022
1500	1018	1101

Figure 4.3 and Table 4.2 present the current versus time plots and corrosion parameters of water-treated stainless steel samples in non-stop tests. The same trend associated with pitting potential and onset time of pitting has been observed from the polarization test. The range associated with pitting potential appears to be relatively consistent for both stop and non-stop water treated samples, which changes from 1.09 V to 1.40 V.

Figure 4.3 (f) shows the current versus potential graph for all grits of water-treated samples in non-stop tests. An increase in pitting potential can be observed from sample G 120 to sample G 1500. Based on previous research [67,69,80,100,103,114–118], active-passive metallic samples with large degree of roughness are more likely to suffer from corrosion, such as pitting on stainless steel. In this case, G 120 samples with relatively rough surfaces are considered to have a higher possibility to be attacked by corrosive ions, and an early onset event with a dramatic spike of current.

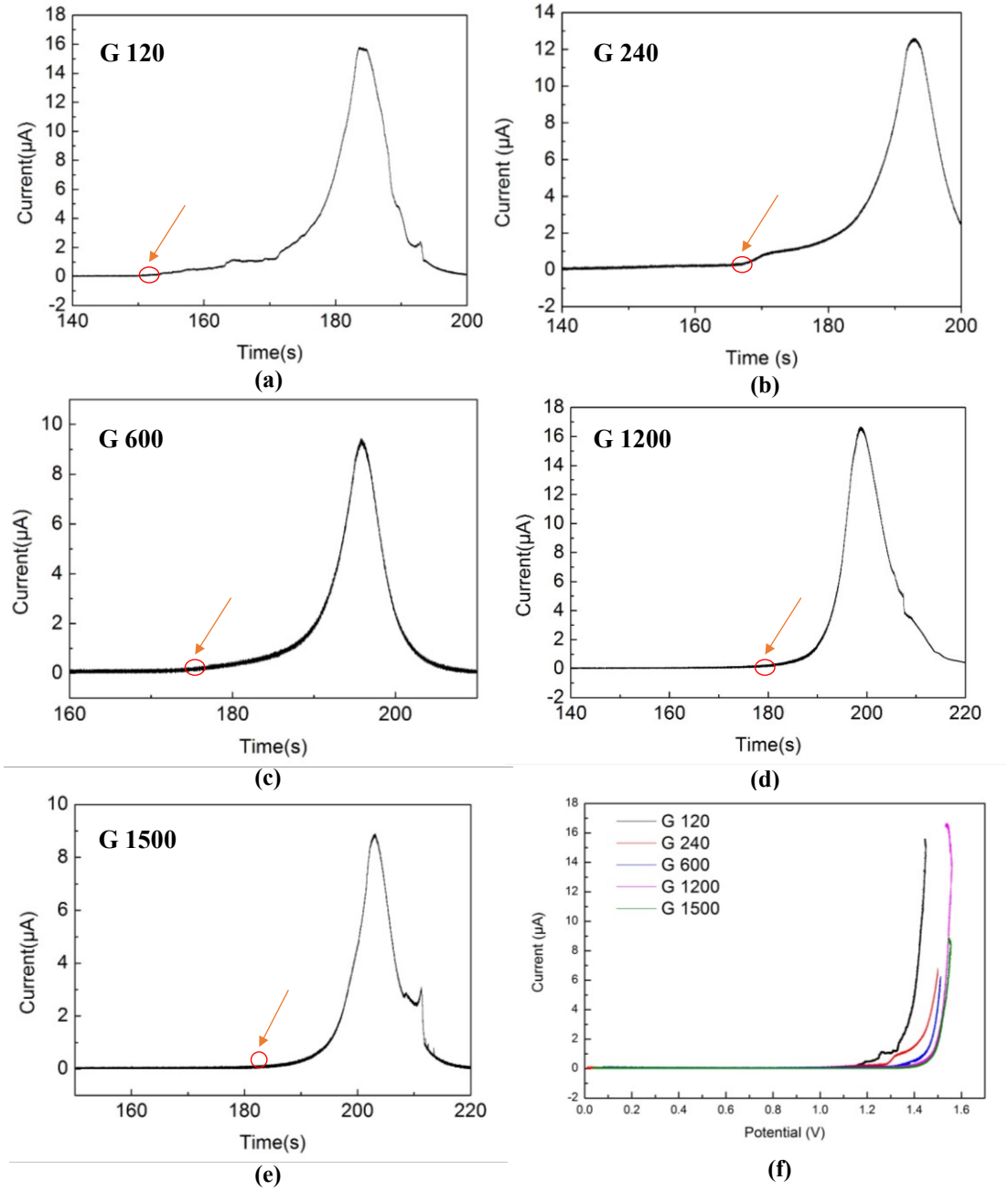

Figure 4.3 The plots of water treated samples in non-stop tests with different surface morphologies. (a)-(e): Current as a function of time for G 120 to G 1500 samples. (f): Current versus potential for G 120 to G 1500 samples.

Figure 4.4 shows the comparison data for four samples, which are G 240 and G 1200 samples with and without water treatment. It is apparent that higher potentials are required for water-treated samples to initiate pitting. For instance, the difference between the potentials for both untreated and water-treated G 240 and G 1200 samples is around 0.2 V. Also, the samples with relatively smooth surfaces (G 1200 samples) are less likely to undergo pitting, and higher potentials are required for them to initiate pitting compared with that of rougher samples (G 240). All the observations suggest that corrosion resistance on smoother surfaces of stainless steel samples is improved by further treating with nanopure water at elevated temperature.

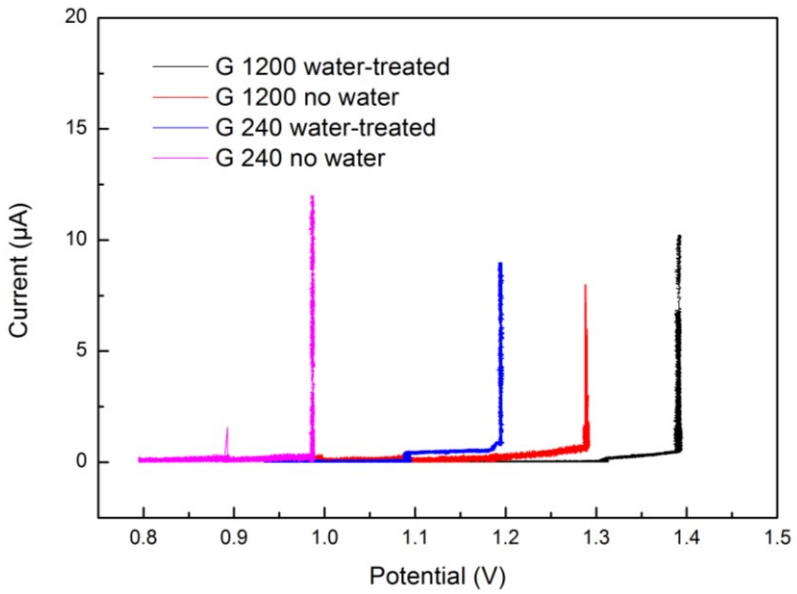

Figure 4.4 The current versus potential for sample G 240 and sample G 1200 with and without water treatment in stop tests.

Details of comparison between water and non-water treated samples are listed in Table 4.2. The changes of corrosion parameters including both the average pitting potentials in two types of anodic polarizations and the average onset time of pitting versus surface roughness with and without water treatment. It appears that samples G

120 and G 240 show relatively significant change in pitting potentials and time, whereas for samples G 1200 and G 1500 with lower surface roughness, effect of water treatment is less intensive than rougher ones. The change (%) in each column has a general decreasing trend by decreasing surface roughness, indicating the influences exerted by surface roughness. Also, taking into account of the samples with same surface roughness, it requires water-treated samples to initiate pitting at higher potentials and a longer time, showing the fact that nanopure water treatment does play a vital role in improving corrosion resistance of stainless steel 316 LVM. On one hand, samples with smoother surfaces and no water treatment had better corrosion performance compared with that of rougher ones, and by treating with water at elevated temperatures, their pitting occurrence and pitting potentials were further improved. On the other hand, corrosion performance of the rougher samples were also enhanced after water treatment. Even though the change (%) of rougher samples were more significant than that of smoother ones, they were still more susceptible to corrosion. All the information in Table 4.2 illustrates the fact that surface roughness and water treatment has a simultaneous effect on the improvement of corrosion resistance of stainless steel samples. The corrosion performance of smoother samples were enhanced and the adding effect of water treatment even postponed their pitting occurrence and increased the pitting potentials. Rougher samples also experienced a better corrosion performance after water treatment. Although the change percentage associated with rougher ones were more significant compared to smooth surfaces, rougher samples were still more susceptible to corrosion compared to smoother ones due to the fact of earlier onset of pitting and lower pitting potentials.

Table 4.2 Comparison between water-treated and non-water treated samples.

Sample	Treatment	$E_{pit\ (non\text{-}stop)}$ /V	$E_{pit(stop)}$ /V	Time/s
G 120	No water	0.83	0.84	600
	Water	1.09	1.09	793
	Change (%)	**31.3**	**29.8**	**32.2**
G 240	No water	1.01	1.02	673
	Water	1.17	1.2	902
	Change (%)	**13.7**	**17.6**	**34.0**
G 600	No water	1.09	1.23	828
	Water	1.27	1.29	918
	Change (%)	**41.2**	**4.9**	**10.9**
G 1200	No water	1.14	1.28	865
	Water	1.38	1.31	931
	Change (%)	**38.0**	**2.3**	**7.6**
G 1500	No water	1.22	1.29	890
	Water	1.4	1.39	1018
	Change (%)	**40.0**	**7.8**	**14.4**

Figure 4.5 shows the error bars for the average pitting potential and initiation time of pitting for samples with different surface finishes in samples with and without water treatment. The ascending trend in both pitting potential and time were found in samples with and without water treatment. As for samples with same surface finishes, corrosion parameters including both potential and initiation time were increased by water treatment. This results demonstrate that the corrosion resistance of stainless steel is enhanced by preparing a smoother surface and it can be further improved by treating those surfaces with a simple nanopure water treatment at elevated temperatures.

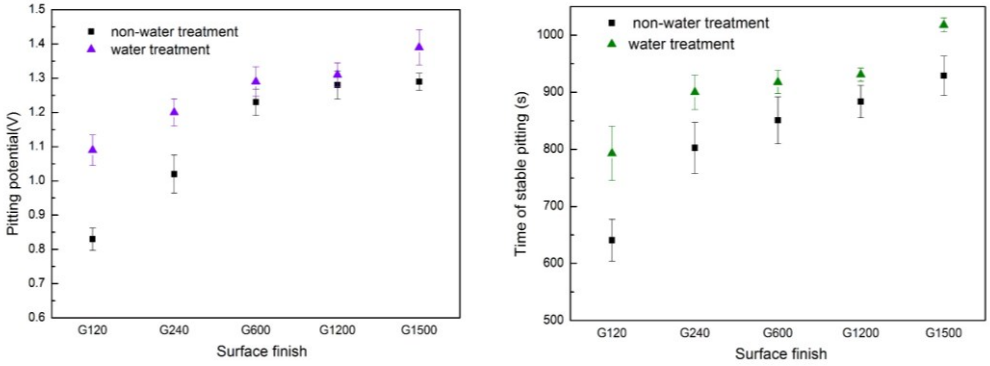

Figure 4.5 Average pitting potential and stable pitting occurrence time for different surface roughness with and without water treatment.

4.4.2 *In-situ* Imaging

Images of *in situ* observations of water-treated and non-water treated samples were obtained by using optical microscope. Figure 4.6 illustrates the images for both water-treated and non-water treated sample G 1200 before and after corrosion. Looking at images between (a) and (c), (b) and (d), there is an obvious change of non-water treated G 1200 sample on the right lower side of the surface after corrosion showing the suspicious formation of pits after corrosion. In contrast, no apparent difference can be seen from water-treated G 1200 sample surface before and after corrosion. This difference in the degree of pitting corrosion can possibly be attributed to the effect exerted by the high temperature water treatment, Klages et al. reported the similar experimental results for the enhancement of corrosion resistance of stainless steel 316 LVM through water treatment with different durations in water bath.

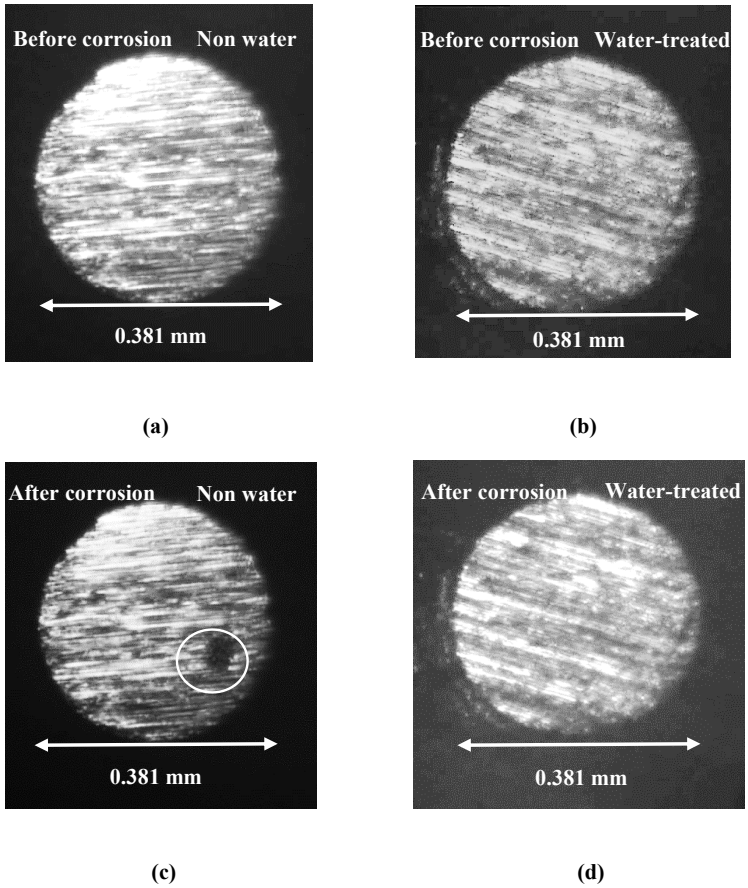

Figure 4.6 *In situ* observations of water-treated and non-water treated G 1200 samples before and after corrosion tests. (a) Sample G 1200 without water treatment before corrosion. (b) With water treatment before corrosion (c) without water treatment after corrosion

4.4.3 SEM and EDS

Scanning electron microscopy (SEM) and energy dispersive X-ray spectroscopy techniques were used to investigate the surface morphology and chemical composition on the surface of the sample. Figure 4.7 shows the SEM micrographs of samples G 240 and G 1200 before and after water treatments. As can be seen from Figure 4.7 (a), (c), (b) and (d), visible pits on sample surfaces were circled and pointed with arrows. Apparently, the total number of circled regions dropped after samples

underwent water treatment, indicating a lower degree of pitting events after treating samples with nanopure water. Sample surfaces were less likely to contain features of abnormalities after water treatment, showing that water treatment could possibly remove the MnS inclusions left on sample surfaces [29]. All these observations indicated that high temperature water treatment could help to remove surface inclusions that are generally considered to be critical cites where pitting initiates [13,21], which further enhanced the corrosion resistance of stainless steels.

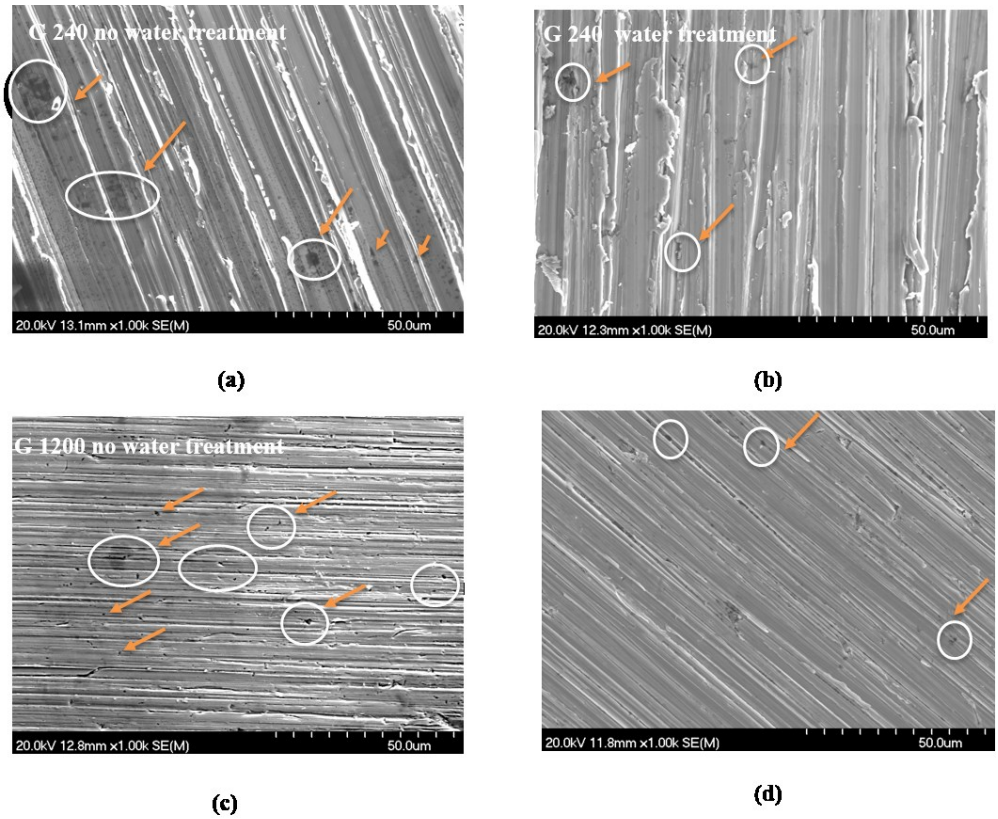

Figure 4.7 SEM images of samples G 240 (a and b) and G 1200 (c and d) with and without water treatment.

EDS measures the change in weight percentage of chemical elements including manganese and sulfur on sample surfaces before and after water treatment. Table 4.3 presents the results obtained for Mn and S content on samples with and without water treatment. By taking a look at the weight percentage for water-treated and non-water treated samples, there is a decreasing trend in both Mn and S content for samples with different surface finishes after water treatment. As can be seen from Table 4.3, the change in percentage of Mn and S stay around (35.5±2) % and (33.3±10) %, respectively. The average value of change (%) in terms of Mn and S content are 36 % and 37.9 %, respectively. The descending trend in both Mn and S content for samples after water treatment suggests that the performance of water treatment lowering the possibility of potential onset of pitting corrosion through the elimination of surface inclusions (MnS). This is in agreement with other research works from Klages et al [29], which demonstrated the enhancement of corrosion resistance of stainless steel samples by water treatment.

Table 4.3 EDS analysis of manganese and sulfur content for stainless steel 316 LVM.

Sample	**Mn (Weight %)**			**S (Weight %)**		
	Water treated	**No water**	**Change (%)**	**Water treated**	**No water**	**Change (%)**
G 120	1.18	1.88	37.2	0.03	0.05	40
G 240	1.2	1.9	36.8	0.04	0.06	33.3
G 600	1.14	1.77	35.5	0.03	0.05	40
G 1200	1.24	1.87	33.7	0.02	0.03	33.3
G 1500	1.15	1.82	36.8	0.04	0.07	42.9
Average	1.18	1.85	36	0.03	0.05	37.9

4.5 DISCUSSION

4.5.1 Effect of High Temperature Water Treatment on Corrosion

The water treatment at elevated temperature also did have an effect on corrosion resistance of stainless steels in terms of the improvement in average pitting potential and the onset time of pitting. A clear observation can be seen from the selected data for the current- time plots associated with the comparison for samples G 240 and G 1200 with and without water treatment, showing the enhancement of corrosion resistance of samples after water treatment. The influence of the water treatment is inversely proportional to the surface smoothness. For relatively smoother samples (G 1200 and G 1500), the influence of water treatment appeared to be less effective than samples with rougher surfaces. In contrast, samples polished with only grit 120 showed large enhancement both in time and average pitting potential with the aid of water treatment. However, due to the fact that it still requires a higher potential for smoother samples to initiate pitting, smoother samples are generally more corrosion resistant to corrosion. This could be interpreted in two aspects. First, MnS is treated as an electronic conductors and could be easily polarized to a potential that could no longer exist thermodynamically, and due to the fact that the electronic conductivity of MnS is lower than that of the metal matrix, the dissolution of MnS occurs preferentially at grain boundaries [22]. Second, rougher samples surfaces tend to have relatively large surface areas [114], which created higher possibility for larger contact areas between nano pure water and samples during water treatment. This could significantly facilitate the dissolution of MnS inclusions from sample surfaces. These inclusions are considered

to be one of the critical sites accounting for the onset of pitting [20,22,23]. The elimination of MnS inclusions on sample surfaces can effectively decrease the critical sites for pits to initiate. Even though no direct evidence can be found in the literaturerelated with the precise analysis about the effect of water treatment on the enhancement of stainless steel samples with different surface morphology, still some previous research work from Klages et al and Bai et al. may support the results obtained in our study [29,119].It is reported from Bai et al. that more inclusions (MnS) were exposed on rougher samples surfaces in nitinol [119]. This supports the fact that water treatment had a relatively significant effect on samples with rougher surfaces, by removing more inclusions from sample surfaces. Also, together with the theory that Klages at el. proposed for the enhancement of corrosion resistance of stainless steel 316 LVM with the dissolution of MnS [29], the improvement in corrosion performance of stainless steel 316 LVM samples in this work can be attributed to the simultaneous effect of both the sample surface morphologies and nanopure water treatment.

4.5.2 Surface Analysis on Corrosion

SEM illustrates difference in the amount of surface anomalies on G 240 and G 1200 before and after water treatment, which could possibly associated with MnS inclusions. It is true that water-treated samples are more likely to have a cleaner surfaces, leaving less visible structures of anomalies on sample surfaces, which to some degree creates a lesser occluded and relatively open surfaces that are less susceptible to corrosion [66]. Corrosion pits were hard to be precisely located by the *in situ* optical microscope in this study. This can be attributed to the appearance of scratches on sample surfaces. Even with the most finely polished samples, it is difficult to compare

the difference in the images recorded at the beginning and end of the electrochemical tests. However, still quite a few of the water-treated and non-water treated samples show relatively distinguishable results from *in situ* images. Samples that were not water-treated experienced higher degree of corrosion due to the formation of more pits on surfaces, whereas no obvious change could be observed for water-treated smoother samples. . This confirms what was obtained in anodic polarization tests for samples with water treatment, showing that corrosion resistance could be improved by decreasing surface roughness and high temperature water treatment on sample surfaces.

4.6 CONCLUSIONS

This study was conducted to investigate the effect of high temperature nanopure water treatment on the corrosion resistance of stainless steel samples with different surface morphologies. An obvious trend with the increase in average pitting potential and initiation time of pitting initiation was observed on both rougher and smoother sample surfaces. The average pitting potential and onset of pitting for the water-treated samples polished with different grit of abrasive SiC papers are higher than the corresponding samples that only went through mechanical grinding. It confirms the fact that, first, the corrosion resistance of samples with a finer surface from mechanical grinding has been improved. Second, water treatment can further assist to the improvement of corrosion resistance of stainless steels 316 LVM samples. Samples with smoother surfaces (G 1200 and G 1500) experienced less enhancement in the pitting potential, and initiation time of pitting than that of rougher ones (G 120) after water treatment. Smoother samples were still considered to be more corrosion resistant due to the fact that it required a higher pitting potential and a longer postponed time for

the onset of pitting. This could be explained with two major factors, including the effect of water treatment and surface morphology. One reason is associated with the property of the electronic conductivity of MnS inclusions leads to a higher probability of polarization to the potential at which they can no longer exist thermodynamically, and further results in an enhancement in dissolution of MnS from sample surfaces with the help of water treatment. Another reason can be accounted for the different surface morphologies, which showing that samples with smoother surface finishes have better corrosion performance. All these factors assist the dissolution of inclusions from metal surfaces, which results in the enhancement of corrosion resistance of stainless steel samples.

CHAPTER 5 CONCLUSIONS AND OUTLOOKS

The projects presented have shown a simple mechanical and environmentally friendly way to enhance the corrosion resistance of stainless steel 316 LVM in biomedical simulated environment. With the assist of in-situ optical microscope and ex-situ surface analysis from SEM, EDS, AFM, and XPS, the information about the alternations on the sample surfaces during the corrosion tests as well as the comparison of sample surfaces before and after corrosion have been obtained.

In the first project, the enhancement of corrosion resistance was done by gradually smoothening the surface through polishing using finer grids of SiC papers, which produced better surfaces with lesser valleys and groves. All samples were imaged with in-situ optical microscope throughout the anodic polarization tests. Due to the fact of morphology of our sample surfaces, which are not mirror-like, it is less likely to obtain useful information with EMSI. However, certain comparable changes on sample surfaces with different grids were captured by optical microscope. Ex situ surface analysis of samples were performed by four other techniques. SEM was used to provide surface images before and after corrosion tests. EDS was performed to give chemical compositions of individual elements on sample surfaces for comparison. The Cl^- and O content were of major interests in the EDS results. A decrease in the content of both of these two chemical elements has been shown when the sample surfaces were smoothened. AFM was further used to provide height and roughness profiles. XPS was used as the identification of chemical species related with naturally–formed passive layers of sample surfaces before and after corrosion. Sample surfaces with finer surface finish are less likely to suffer from pitting corrosion, while corrosion event initiated

relatively fast on rougher surfaces.

The second project was based on the idea and results obtained from the first project. However, the method that was used to improve the corrosion resistance of stainless steel samples was slightly different. Newly polished sample surfaces were bombarded with focused ion beam to create arrays of patterns in terms of small circles with given diameters and distance value of center-to-center circle separations. The most optimal diameters and center-to-center spacing values are 30 micrometers and 60 micrometers, respectively. In order to compare the corrosion resistance of samples with patterns and without. Two types of sample surfaces were created. After those samples underwent the same anodic polarization tests, imaging process with optical microscope and SEM and EDS surface analysis, the results from the tests suggested that the corrosion resistance of samples with arrays of surface patterns have been enhanced significantly compared with samples that simply went through mechanical polishing.

The third project introduced a novel way to further enhance the corrosion resistance of stainless steel samples by high temperature long duration water treatment. Samples wires were first mechanical polished and then immersed in 90 °C nanopure water for 3 hours. The justification of this condition can be explained as followed. First of all, the major role of the water treatment is related with the dissolution of MnS inclusions on sample surfaces to the bulk of the water. Since MnS has generally been considered as the critical inclusions that initiate pitting corrosion of stainless steel alloys [20,22,23], the elimination of MnS inclusions out from the sample surfaces could be a way to depress the possibility for stainless steel to start pitting. Second, both the consideration of 90 °C and 3 hours durations of water treatment is based on the fact

that there will be a higher possibility for the dissolution of MnS into water, which helps to eliminate the total number of the corrosion-triggering sites on the sample surfaces. Increasing the temperature of the surroundings will enhance the thermal motion of molecules. This is the same with this high temperature water treatment; in this case, higher temperatures of water bath will be more likely to get rid of MnS out of the sample surfaces. 90 °C is the upper limit of the temperature chosen for this experiment, due to the fact that the boiling point of water is 100 °C at standard atmosphere. The results shows the fact that the onset of pitting on water treated stainless steel were depressed. Samples with water treatment tend to show a longer postponed time before the initiation of pitting corrosion, an enhanced potential of pitting corrosion and a lower value with regards to the highest critical current, thus, confirming the fact of the enhancement of corrosion resistance of stainless steel samples after high temperature water treatment.

As for future work, still a lot of places can be improved. First, all of the research work has been done so far were related with non-mirror like samples, which left small possibilities for obtaining useful information from EMSI. Thus further work can focus on producing highly smoothened surfaces for the investigation. Second, the simulated biomedical environment in this work is 0.9 % by mass NaCl solutions. However, there are even more choices and simulations of solutions related with mimicking inner body biomedical environment. For instance, Phosphate-buffered saline solutions and Hanks' solution could be candidate solutions, which are of vital interests for the investigation of corrosion performance of stainless steels. Third, due to the limitations of experimental conditions in the lab, corrosion performance of stainless steels in terms

of different temperatures were not considered. This could be another point for further study. Fourth, since the purpose of this research is trying to increase the duration of biomedical implants inside human bodies to withstand corrosion as long as possible, other types of metal alloys besides stainless steels can also be investigated for further inquiry. For instance, titanium and nickel alloys would be another choice. Fifth, due to the fact that the types of corrosion tests provided by the potentioastat in our lab lacks diversity. Lots of other electrochemical tests were not performed on samples. For instance, cyclic voltammetry was tried initially, but it could not provide the similar curves reported from literatures. Hence, further work can be carried out with more exploration of other means of electrochemical tests. The last point to mention is that, modeling was rarely used in our work. However, surface thermodynamics and the deformation and reformation of passive layers related with pit initiation and termination of pits are of vital importance. Thus, modeling on the diffusion process of aggressive ions and thermodynamic process of damage and formation of passive layers of stainless steels could be a new aspect to take into account in future work.

Bibliography

1. N. D. Greene and M. G. Fontana, Corrosion **15**, 41 (1959).

2. G. T. Burstein, C. Liu, R. M. Souto, and S. P. Vines, Corros. Eng. Sci. Technol. **39**, 25 (2004).

3. E. McCafferty, *Introduction to Corrosion Science* (Springer Science & Business Media, 2010).

4. J. Horvath and H. H. Uhlig, J. Electrochem. Soc. **115**, 791 (1968).

5. H. H. Leet and H. H. Uhlig, J. Electrochem. Soc. **117**, 18 (1970).

6. A. Pardo, M. C. Merino, A. E. Coy, F. Viejo, R. Arrabal, and E. Matykina, Corros. Sci. **50**, 1796 (2008).

7. G. O. Ilevbare and G. T. Burstein, Corros. Sci. **43**, 485 (2001).

8. J. R. Galvele, J. B. Lumsden, and R. W. Staehle, J. Electrochem. Soc. **125**, 1204 (1978).

9. R. F. A. Jargelius-Pettersson, Corros. Sci. **41**, 1639 (1999).

10. Y. S. Lim, J. S. Kim, S. J. Ahn, H. S. Kwon, and Y. Katada, Corros. Sci. **43**, 53 (2001).

11. A. J. Sedriks, *Stress Corrosion Cracking Test Methods* (National Association of Corrosion Engineers, 1990).

12. R. W. Hertzberg, (1989).

13. G. S. Frankel, J. Electrochem. Soc. **145**, 2186 (1998).

14. R. P. Frankenthal and H. W. Pickering, J. Electrochem. Soc. **119**, 1304 (1972).

15. P. Marcus and J.-M. Herbelin, Corros. Sci. **34**, 1123 (1993).

16. C. Y. Chao, L. F. Lin, and D. D. Macdonald, J. Electrochem. Soc. **128**, 1187 (1981).

17. L. F. Lin, C. Y. Chao, and D. D. Macdonald, J. Electrochem. Soc. **128**, 1194 (1981).

18. H. H. Strehblow, P. Marcus, and J. Oudar, Corros. Mech. Theory Pract. (1995).

19. W. Khalil, S. Haupt, and H.-H. Strehblow, Mater. Corros. **36**, 16 (1985).

20. T. S. L. Wijesinghe and D. J. Blackwood, Corros. Sci. **49**, 1755 (2007).

21. M. P. Ryan, D. E. Williams, R. J. Chater, B. M. Hutton, and D. S. McPhail, Nature **415**, 770 (2002).

22. G. S. Eklund, J. Electrochem. Soc. **121**, 467 (1974).
23. D. E. Williams, M. R. Kilburn, J. Cliff, and G. I. Waterhouse, Corros. Sci. **52**, 3702 (2010).
24. N. Sato, Electrochimica Acta **16**, 1683 (1971).
25. J. A. Richardson and G. C. Wood, Corros. Sci. **10**, 313 (1970).
26. H. M. Cobb, *The History of Stainless Steel* (ASM International, 2010).
27. J. Beddoes and J. G. Parr, (1999).
28. J. Stewart and D. E. Williams, Corros. Sci. **33**, 457 (1992).
29. P. E. Klages, Z. Bai, M. Lobban, M. K. Rotermund, and H. H. Rotermund, Electrochem. Commun. **15**, 54 (2012).
30. J. E. Castle, Surf. Sci. **68**, 583 (1977).
31. P. E. Klages, M. K. Rotermund, and H. H. Rotermund, Corros. Sci. **65**, 128 (2012).
32. K. M. Lee, H. S. Cho, and D. C. Choi, J. Alloys Compd. **285**, 156 (1999).
33. M. B. González and S. B. Saidman, Corros. Sci. **53**, 276 (2011).
34. A. M. Slaney, V. A. Wright, P. J. Meloncelli, K. D. Harris, L. J. West, T. L. Lowary, and J. M. Buriak, ACS Appl. Mater. Interfaces **3**, 1601 (2011).
35. H. Lim, P. Kim, H. Jeong, and S. Jeong, J. Mater. Process. Technol. **212**, 1347 (2012).
36. P. Peyre, X. Scherpereel, L. Berthe, C. Carboni, R. Fabbro, G. Beranger, and C. Lemaitre, Mater. Sci. Eng. A **280**, 294 (2000).
37. C.-C. Shih, C.-M. Shih, Y.-Y. Su, L. H. J. Su, M.-S. Chang, and S.-J. Lin, Corros. Sci. **46**, 427 (2004).
38. A. J. Bard, L. R. Faulkner, J. Leddy, and C. G. Zoski, *Electrochemical Methods: Fundamentals and Applications* (Wiley New York, 1980).
39. R. J. Flanagan, D. Perrett, and R. Whelpton, *Electrochemical Detection in HPLC: Analysis of Drugs and Poisons* (Royal Society of Chemistry, 2005).
40. P. E. Klages, (2012).
41. C. Punckt, M. Bölscher, H. H. Rotermund, A. S. Mikhailov, L. Organ, N. Budiansky, J. R. Scully, and J. L. Hudson, Science **305**, 1133 (2004).
42. K. D. Vernon-Parry, III-Vs Rev. **13**, 40 (2000).

43. C. R. Brundle, C. A. Evans, and S. Wilson, *Encyclopedia of Materials Characterization: Surfaces, Interfaces, Thin Films* (Gulf Professional Publishing, 1992).
44. R. Van Grieken and A. Markowicz, *Handbook of X-Ray Spectrometry* (CRC Press, 2001).
45. J. C. Russ, *Fundamentals of Energy Dispersive X-Ray Analysis: Butterworths Monographs in Materials* (Butterworth-Heinemann, 2013).
46. H.-J. Butt, B. Cappella, and M. Kappl, Surf. Sci. Rep. **59**, 1 (2005).
47. G. Binnig, C. F. Quate, and C. Gerber, Phys. Rev. Lett. **56**, 930 (1986).
48. J. F. Watts and J. Wolstenholme, Introd. Surf. Anal. XPS AES John F Watts John Wolstenholme Pp 224 ISBN 0-470-84713-1 Wiley-VCH May 2003 224 (2003).
49. J. F. Moulder, J. Chastain, and R. C. King, *Handbook of X-Ray Photoelectron Spectroscopy: A Reference Book of Standard Spectra for Identification and Interpretation of XPS Data* (Physical Electronics Eden Prairie, MN, 1995).
50. D. Chattarji, *The Theory of Auger Transitions" P 43-44 Academic Press* (London, 1976).
51. P. Wang, D. Zhang, and R. Qiu, Corros. Sci. **54**, 77 (2012).
52. K. L. Mittal, *Contact Angle, Wettability and Adhesion* (CRC Press, 2006).
53. T. Young, Philos. Trans. R. Soc. Lond. 65 (1805).
54. A. S. Toloei, V. Stoilov, and D. O. Northwood, Appl. Surf. Sci. **284**, 242 (2013).
55. X. J. Feng and L. Jiang, Adv. Mater. **18**, 3063 (2006).
56. R. N. Wenzel, Ind. Eng. Chem. **28**, 988 (1936).
57. A. B. D. Cassie and S. Baxter, Trans. Faraday Soc. **40**, 546 (1944).
58. W. Tian, N. Du, S. Li, S. Chen, and Q. Wu, Corros. Sci. **85**, 372 (2014).
59. F. A. Martin, C. Bataillon, and J. Cousty, Corros. Sci. **50**, 84 (2008).
60. R. Z. Zand, K. Verbeken, and A. Adriaens, Prog. Org. Coat. **72**, 709 (2011).
61. A. S. Toloei, S. Atashin, and M. E. Bahrololoom, Mater.Perform **52**, 38 (2013).
62. L. Zhang, W. Zhang, Y. Jiang, B. Deng, D. Sun, and J. Li, Electrochimica Acta **54**, 5387 (2009).
63. F. Zhang, E. T. Kang, K. G. Neoh, P. Wang, and K. L. Tan, Biomaterials **22**, 1541 (2001).

64. W. Liang, Appl. Surf. Sci. **211**, 308 (2003).
65. K. Sasaki and G. T. Burstein, Corros. Sci. **38**, 2111 (1996).
66. G. T. Burstein and P. C. Pistorius, Corrosion **51**, 380 (1995).
67. G. T. Burstein and S. P. Vines, J. Electrochem. Soc. **148**, B504 (2001).
68. A. S. Toloei, V. Stoilov, and D. O. Northwood, CMEM **2**, 243 (2014).
69. Toloei, A. S., Stoilov, V., and Northwood, D. O., WIT. Trans. Eng. Sci **77**, 193 (2013).
70. T. Hong and M. Nagumo, Corros. Sci. **39**, 1665 (1997).
71. J. Beddoes and K. Bucci, J. Mater. Sci. Mater. Med. **10**, 389 (1999).
72. O. Cisse, O. Savadogo, M. Wu, and L. Yahia, J. Biomed. Mater. Res. **61**, 339 (2002).
73. M. Kaczmarek, W. Simka, A. Baron, J. Szewczenko, and J. Marciniak, J. Achiev. Mater. Manuf. Eng. **18**, (2006).
74. W. Li and D. Y. Li, Acta Mater. **54**, 445 (2006).
75. M. Cabrini, A. Cigada, G. Rondell, and B. Vicentini, Biomaterials **18**, 783 (1997).
76. T. Suter, Y. Müller, P. Schmutz, and O. von Trzebiatowski, Adv. Eng. Mater. **7**, 339 (2005).
77. R. Walter and M. B. Kannan, Mater. Des. **32**, 2350 (2011).
78. M. Dornhege, C. Punckt, J. L. Hudson, and H. H. Rotermund, J. Electrochem. Soc. **154**, C24 (2007).
79. Y. Zuo, H. Wang, and J. Xiong, Corros. Sci. **44**, 25 (2002).
80. S. M. Lee, W. G. Lee, Y. H. Kim, and H. Jang, Corros. Sci. **63**, 404 (2012).
81. J. B. Park and J. D. Bronzino, *Biomaterials: Principles and Applications* (crc press, 2002).
82. M. Niinomi, Metall. Mater. Trans. A **33**, 477 (2002).
83. J. Pan, C. Leygraf, D. Thierry, and A. M. Ektessabi, J. Biomed. Mater. Res. **35**, 309 (1997).
84. Y. Xin, C. Liu, X. Zhang, G. Tang, X. Tian, and P. K. Chu, J. Mater. Res. **22**, 2004 (2007).
85. Y. Xin, C. Liu, K. Huo, G. Tang, X. Tian, and P. K. Chu, Surf. Coat. Technol. **203**, 2554 (2009).

86. S. Virtanen, I. Milošev, E. Gomez-Barrena, R. Trebše, J. Salo, and Y. T. Konttinen, Acta Biomater. **4**, 468 (2008).
87. H. R. A. Bidhendi and M. Pouranvari, Metall. Mater. Eng. **17**, 13 (2011).
88. E. Marin, A. Lanzutti, L. Guzman, and L. Fedrizzi, J. Coat. Technol. Res. **8**, 655 (2011).
89. M. G. Fontana, *Corrosion Engineering* (Tata McGraw-Hill Education, 2005).
90. L. Chenglong, Y. Dazhi, L. Guoqiang, and Q. Min, Mater. Lett. **59**, 3813 (2005).
91. C. Liu, G. Lin, D. Yang, and M. Qi, Surf. Coat. Technol. **200**, 4011 (2006).
92. F. T. Cheng, K. H. Lo, and H. C. Man, Surf. Coat. Technol. **172**, 316 (2003).
93. S. M. Hosseinalipour, A. Ershad-Langroudi, A. N. Hayati, and A. M. Nabizade-Haghighi, Prog. Org. Coat. **67**, 371 (2010).
94. J. Gallardo, A. Duran, and J. J. De Damborenea, Corros. Sci. **46**, 795 (2004).
95. T. P. Chou, C. Chandrasekaran, and G. Z. Cao, J. Sol-Gel Sci. Technol. **26**, 321 (2003).
96. M. L. Zheludkevich, I. M. Salvado, and M. G. S. Ferreira, J. Mater. Chem. **15**, 5099 (2005).
97. M. Talha, C. K. Behera, and O. P. Sinha, Mater. Sci. Eng. C **33**, 3563 (2013).
98. A. Shahryari, S. Omanovic, and J. A. Szpunar, Mater. Sci. Eng. C **28**, 94 (2008).
99. A. Shahryari and S. Omanovic, Electrochem. Commun. **9**, 76 (2007).
100. A. Toloei, V. Stoilov, and D. Northwood, in *ASME 2013 Int. Mech. Eng. Congr. Expo.* (American Society of Mechanical Engineers, 2013), pp. V02BT02A054–V02BT02A054.
101. R. S. Bedi, D. E. Beving, L. P. Zanello, and Y. Yan, Acta Biomater. **5**, 3265 (2009).
102. R. Hauert, Diam. Relat. Mater. **12**, 583 (2003).
103. A. Toloei, V. Stoilov, and D. Northwood, in *ASME 2012 Int. Mech. Eng. Congr. Expo.* (American Society of Mechanical Engineers, 2012), pp. 1297–1303.
104. W. Xi, Z. Qiao, C. Zhu, A. Jia, and M. Li, Appl. Surf. Sci. **255**, 4836 (2009).
105. A. Marmur, Langmuir **24**, 7573 (2008).
106. A. Marmur, Langmuir **19**, 8343 (2003).

107. V. Vaikuntanathan, R. Kannan, and D. Sivakumar, Colloids Surf. Physicochem. Eng. Asp. **369**, 65 (2010).
108. A. Toloei, M. Guo, and H. H. Rotermund, J. Mater. Eng. Perform. **24**, 3726 (2015).
109. N. Aouina, F. Balbaud-Célérier, F. Huet, S. Joiret, H. Perrot, F. Rouillard, and V. Vivier, Electrochimica Acta **56**, 8589 (2011).
110. G. Wranglen, Corros. Sci. **14**, 331 (1974).
111. R. Qvarfort, Corros. Sci. **40**, 215 (1998).
112. N. J. Laycock and R. C. Newman, Corros. Sci. **39**, 1771 (1997).
113. A. A. Hermas, Prog. Org. Coat. **61**, 95 (2008).
114. G. T. Burstein and P. C. Pistorius, Corrosion **51**, 380 (1995).
115. T. Hong and M. Nagumo, Corros. Sci. **39**, 1665 (1997).
116. A. S. Toloei, V. Stoilov, and D. O. Northwood, Appl. Surf. Sci. **284**, 242 (2013).
117. A. S. Toloei, V. Stoilov, and D. O. Northwood, CMEM **2**, 243 (2014).
118. A. S. Toloei, V. Stoilov, and D. O. Northwood, Mater. Characterisation VII **90**, 355 (2015).
119. Z. Bai and H. H. Rotermund, J. Biomed. Mater. Res. B Appl. Biomater. **99**, 1 (2011).

Appendix A

Copyright Permission

This appendix contains the copyright permissions required to reprint published material.

C.1 Springer License Term and Conditions

This is a License Agreement between Mengnan Guo ("You") and Springer ("Springer") provided by Copyright Clearance Center ("CCC"). The license consists of your order details, the terms and conditions provided by Springer, and the payment terms and conditions.

All payments must be made in full to CCC. For payment instructions, please see information listed at the bottom of this form.

License Number	3806551045887
License date	Feb 12, 2016
Licensed content publisher	Springer
Licensed content publication	Journal of Materials Engineering and Performance
Licensed content title	The Effect of Surface Morphology on Corrosion Performance of SS316 LVM Biomedical Devices
Licensed content author	Alisina Toloei
Licensed content date	Jan 1, 2015

Volume number	24
Issue number	10
Type of Use	Thesis/Dissertation
Portion	Full text
Number of copies	1
Author of this Springer article	Yes and you are a contributor of the new work
Order reference number	None
Title of your thesis / dissertation	Enhancing Corrosion Resistance of Stainless Steel 316LVM by Various Surface Modifications in Biomedical Devices
Expected completion date	May 2016
Estimated size (pages)	100
Total	0.00 CAD

Terms and Conditions

Introduction

The publisher for this copyrighted material is Springer. By clicking "accept" in connection with completing this licensing transaction, you agree that the following terms and conditions apply to this transaction (along with the Billing and Payment terms and conditions established by Copyright Clearance Center, Inc. ("CCC"), at the time that you opened your Rightslink account and that are available at any time at http://myaccount.copyright.com).

General Terms

Limited License: With reference to your request to reuse material on which Springer controls the copyright, permission is granted for the use indicated in your enquiry under the following conditions: Licenses are for one-time use only with a maximum distribution equal to the number stated in your request. Springer material represents original material which does not carry references to other sources. If the material in question appears with a credit to another source, this permission is not valid and authorization has to be obtained from the original copyright holder.

This permission

- is non-exclusive
- is only valid if no personal rights, trademarks, or competitive products are infringed.
- explicitly excludes the right for derivatives.

- Springer does not supply original artwork or content.
- According to the format which you have selected, the following conditions apply accordingly:

- **Print and Electronic:** This License include use in electronic form provided it is password protected, on intranet, or CD-Rom/DVD or E-book/E-journal. It may not be republished in electronic open access.
- **Print:** This License excludes use in electronic form.
- **Electronic:** This License only pertains to use in electronic form provided it is password protected, on intranet, or CD-Rom/DVD or E-book/E-journal. It may not be republished in electronic open access.

For any electronic use not mentioned, please contact Springer at permissions.springer@spi- global.com.

- Although Springer controls the copyright to the material and is entitled to negotiate on rights, this license is only valid subject to courtesy information to the author (address is given in the article/chapter).
- If you are an STM Signatory or your work will be published by an STM Signatory and you are requesting to reuse figures/tables/illustrations or single text extracts, permission is granted according to STM Permissions Guidelines: http://www.stm-assoc.org/permissions- guidelines/

For any electronic use not mentioned in the Guidelines, please contact Springer at permissions.springer@spi-global.com. If you request to reuse more content than stipulated in the STM Permissions Guidelines, you will be charged a permission fee for the excess content.

Permission is valid upon payment of the fee as indicated in the licensing process. If permission is granted free of charge on this occasion that does not prejudice any rights we might have to charge for reproduction of our copyrighted material in the future.

- If your request is for reuse in a Thesis, permission is granted free of charge under the following conditions:

This license is valid for one-time use only for the purpose of defending your thesis and with a maximum of 100 extra copies in paper. If the thesis is going to be published, permission needs to be reobtained.

- includes use in an electronic form, provided it is an author-created version of the thesis on his/her own website and his/her university's repository, including

UMI (according to the definition on the Sherpa website: http://www.sherpa.ac.uk/romeo/);

- is subject to courtesy information to the co-author or corresponding author.

Geographic Rights: Scope

Licenses may be exercised anywhere in the world. Altering/Modifying Material: Not Permitted

Figures, tables, and illustrations may be altered minimally to serve your work. You may not alter or modify text in any manner. Abbreviations, additions, deletions and/or any other alterations shall be made only with prior written authorization of the author(s).

Reservation of Rights

Springer reserves all rights not specifically granted in the combination of (i) the license details provided by you and accepted in the course of this licensing transaction and (ii) these terms and conditions and (iii) CCC's Billing and Payment terms and conditions.

License Contingent on Payment

While you may exercise the rights licensed immediately upon issuance of the license at the end of the licensing process for the transaction, provided that you have disclosed complete and accurate details of your proposed use, no license is finally effective unless and until full payment is received from you (either by Springer or by CCC) as provided in CCC's Billing and Payment terms and conditions. If full payment is not received by the date due, then any license preliminarily granted shall be deemed automatically

revoked and shall be void as if never granted. Further, in the event that you breach any of these terms and conditions or any of CCC's Billing and Payment terms and conditions, the license is automatically revoked and shall be void as if never granted. Use of materials as described in a revoked license, as well as any use of the materials beyond the scope of an unrevoked license, may constitute copyright infringement and Springer reserves the right to take any and all action to protect its copyright in the materials. Copyright Notice: Disclaimer

You must include the following copyright and permission notice in connection with any reproduction of the licensed material:

"Springer book/journal title, chapter/article title, volume, year of publication, page, name(s) of author(s), (original copyright notice as given in the publication in which the material was originally published) "With permission of Springer"

In case of use of a graph or illustration, the caption of the graph or illustration must be included, as it is indicated in the original publication.

Warranties: None

Springer makes no representations or warranties with respect to the licensed material and adopts on its own behalf the limitations and disclaimers established by CCC on its behalf in its Billing and Payment terms and conditions for this licensing transaction.

Indemnity

You hereby indemnify and agree to hold harmless Springer and CCC, and their respective officers, directors, employees and agents, from and against any and all

claims arising out of your use of the licensed material other than as specifically authorized pursuant to this license.

No Transfer of License

This license is personal to you and may not be sublicensed, assigned, or transferred by you without Springer's written permission.

No Amendment Except in Writing

This license may not be amended except in a writing signed by both parties (or, in the case of Springer, by CCC on Springer's behalf).

Objection to Contrary Terms

Springer hereby objects to any terms contained in any purchase order, acknowledgment, check endorsement or other writing prepared by you, which terms are inconsistent with these terms and conditions or CCC's Billing and Payment terms and conditions. These terms and conditions, together with CCC's Billing and Payment terms and conditions (which are incorporated herein), comprise the entire agreement between you and Springer (and CCC) concerning this licensing transaction. In the event of any conflict between your obligations established by these terms and conditions and those established by CCC's Billing and Payment terms and conditions, these terms and conditions shall control.

Jurisdiction

All disputes that may arise in connection with this present License, or the breach thereof, shall be settled exclusively by arbitration, to be held in the Federal Republic of Germany, in accordance with German law. V 12AUG2015

customercare@copyright.com or +1-855-239-3415 (toll free in the US) or +1-978-646-2777.